System Modelling and Improvements of a Mixed Analog Digital Chip for Ionization Chamber Readout in Static and Pulsed Fields

Electrical and Electronic Section - Master's Thesis

Clyde Laforge

Under the supervision of
Dr. Hamza Boukabache & Prof. Andreas Peter Burg

Carried out at the Instrumentation Section
Occupational Health & Safety and Environmental Protection Unit
CERN
Handed on the 18th March 2022

Contents

1 Introduction **4**

1.1 CERN . . . 4

1.2 Radiation Exposure . . . 5

1.3 Need for Radiation Monitoring at CERN . . . 5

1.4 Current Radiation Monitoring System: CROME . . . 6

1.4.1 Ionization Chamber . . . 7

1.4.2 Front-End Electronics . . . 9

1.4.3 Processing and Interface . . . 10

1.4.4 Functional Requirements for CROME . . . 11

1.5 Motivation For This Work . . . 11

2 The Accurate 2A ASIC **13**

2.1 Non-Saturating regime . . . 15

2.1.1 Current Integration . . . 15

2.1.2 Charge Pump Connection . . . 16

2.1.3 Finding the Steady State . . . 18

2.1.4 Values of Interest and Theoretical Results . . . 19

2.2 Saturating Regime . . . 22

2.2.1 LTI Modelling of Accurate in the Saturating Regime . . . 22

2.2.2 Theoretical Results . . . 23

3 Improving on Accurate 2A **25**

3.1 Imperfection of Real Components . . . 25

3.2 Single Capacitor . . . 26

3.2.1 Non-Saturating Regime . . . 26

3.2.2 Saturating Regime . . . 28

3.3 Simple Twin Accurate . . . 29

3.4 Capacitor Ladder . . . 30

3.4.1 Non-saturating Regime . . . 30

3.4.2 Saturating Regime . . . 33

3.5 Twin Accurate . . . 34

4 Design of the New Testboards **35**

4.1 Input Circuitry . . . 35

4.1.1 Component Values Chosen . . . 36

4.2 Additional Devices . . . 36

4.3 Interface with the Zynq Platform . . . 36

5 CROME Integration **37**

5.1 Change of Carrier Board . . . 37

5.2 I2C Devices . . . 37
5.2.1 Master . . . 38
5.2.2 SHT21 Controller . . . 38
5.2.3 DACs Controller . . . 38
5.2.4 Arbiter . . . 38
5.3 Accurate 2 . . . 39
5.3.1 Accurate Frontend . . . 39
5.3.2 Clock Domain Crossing (CDC) . . . 40
5.3.3 Alternative to Regular Front-End . . . 41
5.4 PS to PL Modifications . . . 42

6 Measurements **43**
6.1 HSE-RP-IL (CERN) . . . 43
6.1.1 Calibration . . . 43
6.1.2 Non-Saturating Accuracy . . . 43
6.2 Calibration Laboratory . . . 46
6.2.1 Static Accuracy . . . 46
6.3 IRA (CHUV) . . . 48
6.3.1 The Oriatron eRT6 Accelerator . . . 49
6.3.2 Metaparameters Selection . . . 49
6.3.3 Pulsed Accuracy . . . 50
6.3.4 An Electrical Approach to Ionization Chambers in Pulsed Regime . . . 53
6.4 Single Pulse Evaluation . . . 58

7 Conclusion and Outlook **61**

A Numerical Values **65**

B Detailed solution for bareAccurate in static operation, during the Charge Pump Connection **66**

C Detailed solution for capAccurate in static operation, during the Charge Pump Connection **67**

D Detailed solution for capAccurate in static operation, during the Current Integration **68**

E IRA Additional Graphs **68**

Acknowledgements

The successful completition of thesis thesis was the result of the support of many people from CERN, EPFL and outside. I want to thank my supervisors Dr. Hamza Boukabache (CERN) and Prof. Andreas Peter Burg (EPFL), who trusted me with their time and gave me key advice which shaped my thesis. I would also like thank them for their flawless reactivity when time was tight. I further want to thank Dr. Hamza Boukabache for his close collaboration and support. I would like to thank Dr. Sarath Kundumattathil Mohanan for all the precious insights and motivation around this thesis' subject. The help of both Dr. Hamza Boukabache and Dr. Sarath Kundumattathil Mohanan went above and beyond and even into the weekends.

I would like to thank Daniel Perrin for welcoming me in the section, as well as his constant kindness and interest. I further want to thank the whole CROME team for the advice and discussion. Gaël was always ready to share solutions to my day to day issues or questions, ranging from PCB design to CROME's infrastructure, passing by VHDL design. Jonas was there for interesting discussion and and giving a precious second opinion on many hypothesis I had. Michel shared his long experience with radiation measurement devices and pushed me to dig deeper. Special thanks to colleagues from BE-CEM for the PCB design and manufacturing, in particular Raphael Berberat, without whom the prototype boards would have never been ready soon enough to allow for proper testing.

I also want to thank the section's administrative staff, especially Marta Alegria Bernal and Roxana Cristina Banica for bearing with the incessant urgency of my requests. Furthermore, I want to thank the Institute of Radiation Physics (IRA) for allowing the testing of the prototypes on their facilities. I also want to thank Geyer Walter Reiner in particular for sharing his excellent knowledge in radiation dosimetry, as well as his spirited enthusiasm for the subject.

Furthermore, I want to thank all my familly members and partner, who supported me through all the stressful times during my master courses and thesis.

1 Introduction

1.1 CERN

CERN, the European Organization for Nuclear Research, is a unique research facility designed to understand the basic constituents of matter by colliding particles traveling at a extremely high speeds. A series of accelerators have been built at CERN to push the particles extremely close to the speed of light, reaching energy levels of up to $6.5 TeV$[1]. The particles then collide at arbitrary locations, where the resulting byproducts are studied in the aim to further knowledge about the subatomic world and the laws of nature.

An overview of CERN's facilities is shown in figure 1.

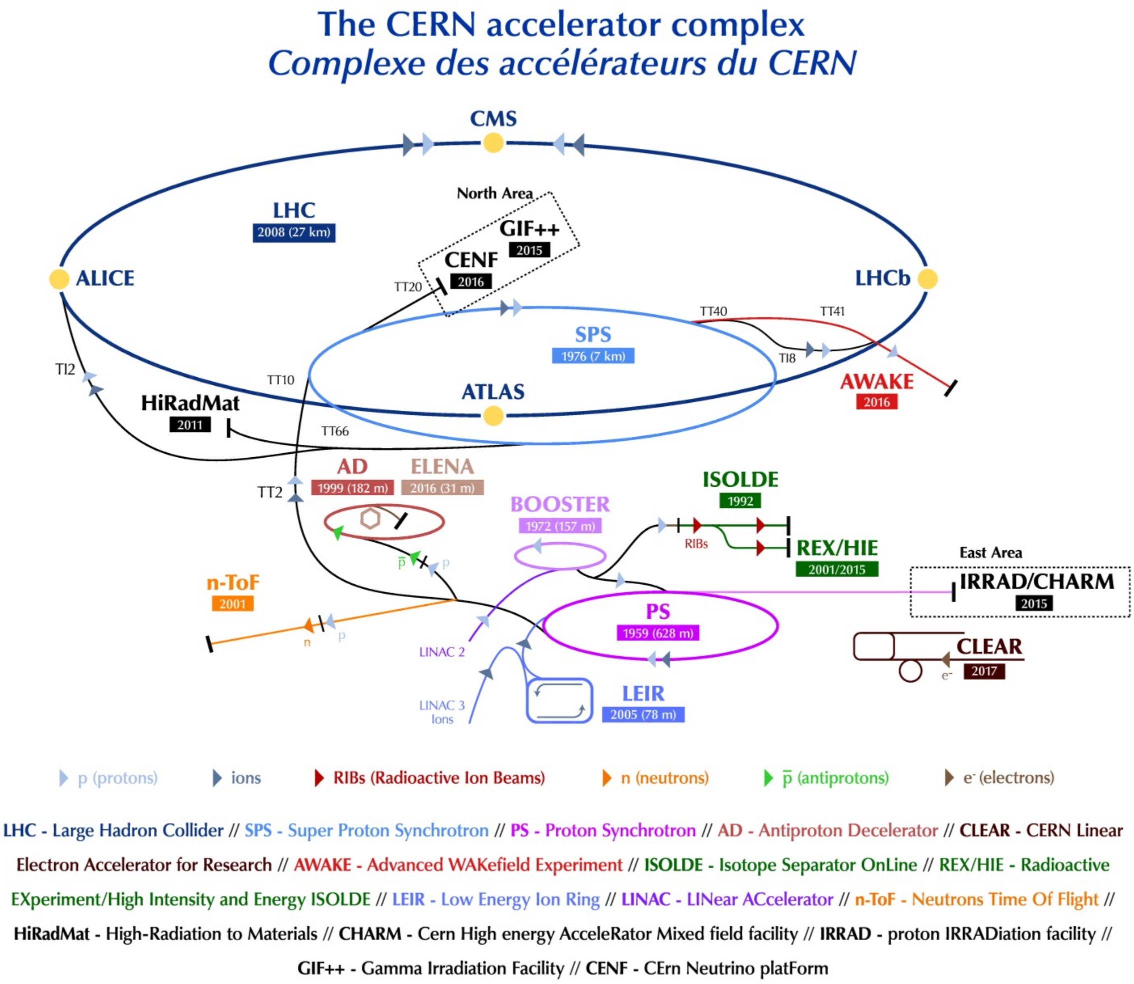

Figure 1: The CERN accelerator complex in 2018[2]

The path of the particles start from a bottle of hydrogen, where ions are extracted and fed to $Linac4$, a linear accelerator, which accelerates them to $160\,\mathrm{MeV}$, preparing them for their injection to the next stage, the Proton Synchrotron Booster (PSB)[3][4]. Inside the PSB, the ions are accelerated to $2\,\mathrm{GeV}$[5] and fed to the Proton Synchrotron (PS) and then to the Super Proton Synchrotron (SPS), pushing the energy further with each stage. The ions then reach the Large Hadron Collider (LHC) and end up an energy level of $6.5\,\mathrm{TeV}$[1]. There are two beam pipes inside of the LHC, where the particles travel in opposite direction. The beams finally collide inside of one of four detectors - ALICE, ATLAS, CMS and LHCb. Because two beams with opposite orientation are used, the total energy at the collision point is multiplied by two and reaches $13\,\mathrm{TeV}$. It is worth noting that the beam can be redirected at different stages, providing it for different experiments (nTOF, ISOLDE, and more).

1.2 Radiation Exposure

In dosimetry, the ionization radiation, most often referred to as simply radiation, consists of subatomic particles or electromagnetic waves with the ability to ionize matter. This property is central to the biological consequences, which range from no impact to radiation burns, radiation sickness or death depending on the exposure[6]. As the physical interaction of ionizing radiation varies depending on the particles, energy levels and target matter, the need to describe the consequences of exposure in a way which is agnostic to the specificity of a particular type of radiation arose. Because many effects are expected to scale with the absorbed energy per unit mass, the *absorbed dose* D with unit *gray* (Gy) was introduced[7]:

$$1\,\mathrm{Gy} = 1\,\frac{\mathrm{J}}{\mathrm{kg}} \tag{1}$$

However, the absorbed dose is not the only factor to take into account, as different absorbed doses of the same value may not have the same biological consequences. For example a certain absorbed dose received over multiple year, where the tissue can repair damage as times goes on and the same dose delivered over a few seconds are bound to have different consequences. The concept that links a certain radiation exposure to biological effect is called the *dose equivalent* H, which is the absorbed dose multiplied by the quality factor, Q (dimensionless) .

$$H = DQ \tag{2}$$

This means that two different exposure to ionizing radiation with the same dose equivalent yield the same biological effects.

While the dose equivalent has the same dimensions that the absorbed dose, a different unit has been associated to it to avoid confusion, the *sievert* (Sv). The evaluation of Q depending on the type of ionizing radiation is non trivial, and will be left out of this thesis.

1.3 Need for Radiation Monitoring at CERN

During CERN's operation, a particle beam may collide with another, hit a target, or suffer losses. Any time such a thing happens, high energy particles will interact with matter. One of the consequences is the apparition of a secondary field, commonly called stray radiation. Depending on the beam activity, as well as the material surrounding the event, some amount of matter around the area might get unstable (i.e activated), resulting in detectable dose rates well after the end of operations. The resulting secondary field is called stray radiation depicted in figure 2.[8]

Because of these effects, the ambient dose is constantly monitored and access to areas is allowed only when the levels are deemed safe. Moreover, as collisions and events surrounding the accelerator may happen very fast, the profile of ionization radiation may vary wildly, with intense, highly pulsed fields during operation, and much lower, quasi-constant fields afterward.

For complex facilities such as CERN, radiation protection has three main objectives:

- Protecting the CERN's equipment, including the different parts of the accelerators.
- Protecting CERN's personnel.

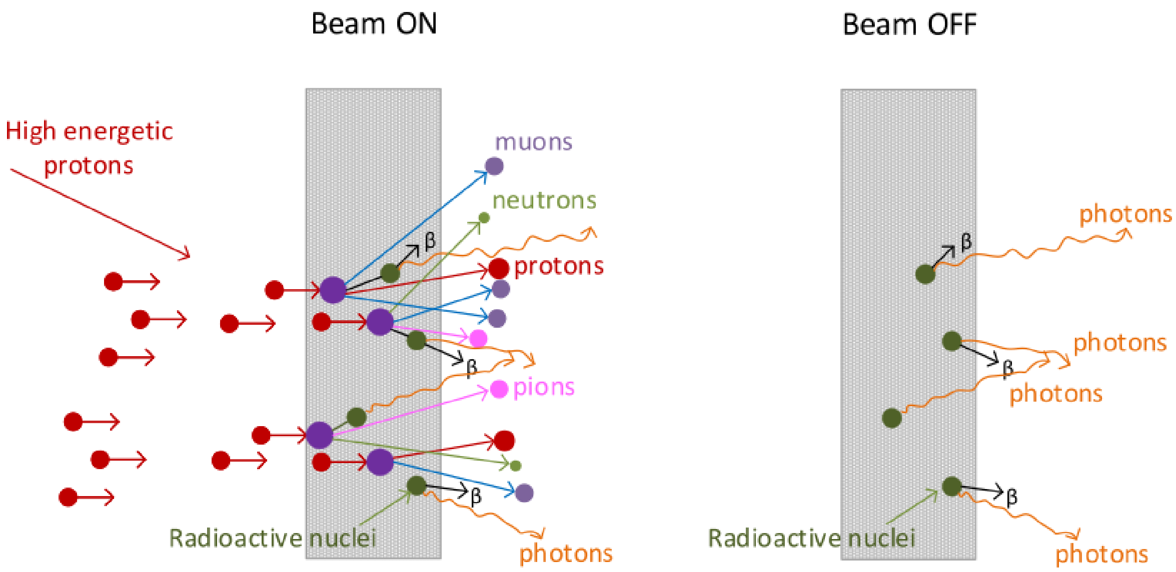

Figure 2: Stray radiation produced by accelerated protons[9]

- Protecting the environment.

Due to the differences of challenges in the protection of the equipment on the one hand and the protection of the personnel and environment on the other hand, two different and independent systems are used. In the first line of defense comes the Machine Protection System (MPS), which monitors CERN's equipment with the main objective to protect the machine, protect the beam and provide evidence in case of failure[10]. This system operates with an interlock mechanism, where a multitude of agents ($\sim 10'000$) can request the operations to be stopped[11]. Due to the high energy contained inside the beam, aborting operation is not a trivial task as this energy has to be disposed of somehow. This process is called "beam dump".

The Personnel Protection System (PPS) is focused on the protection of the personnel and environment. Part of this strategy are the monitors provided by the Radiation Protection (RP) group, which are installed at various key locations at CERN. These monitors provide continuous data logging to a central supervision (REMUS) and may produce audio and visual alarms, as well as interface to the interlock system, depending on the the context.

1.4 Current Radiation Monitoring System: CROME

A typical radiation monitoring system for is depicted in figure 3. The radiation sensor may be one of many kinds, such as a neutron counter, scintillator, ionization chamber, ... [7]. The read out electronics makes sense from the sensor and produces a digital value, readable by the processing unit. The most critical job of the processing unit is to extract information about the dose equivalent and trigger an interlock and/or alarm if a safety threshold has been crossed. The safety criterion is used for the monitoring system is either based on a running average of the dose rate, or the total dose[1] over consecutive intervals. It is worth noting that while the data storage and supervision is important for monitoring, debugging and understanding the events, it is *not* part of the safety critical system, meaning that the system must keep working even if the communication is broken.

While such a radiation monitoring system can exist with a multitude of different sensors, electronics and processing units, the following will focus on the current system developed in

[1]equal to the integrated dose rate

CERN's Instrumentation Laboratory, part of the Radiation Protection (RP), CROME. CROME uses an ionization chamber as the radiation sensor, a reset counting method based on current integration for the front-end electronics, and a Zynq System on Chip (SoC) for the processing. Because of its complexity, some aspects of the device may be simplified or omitted.

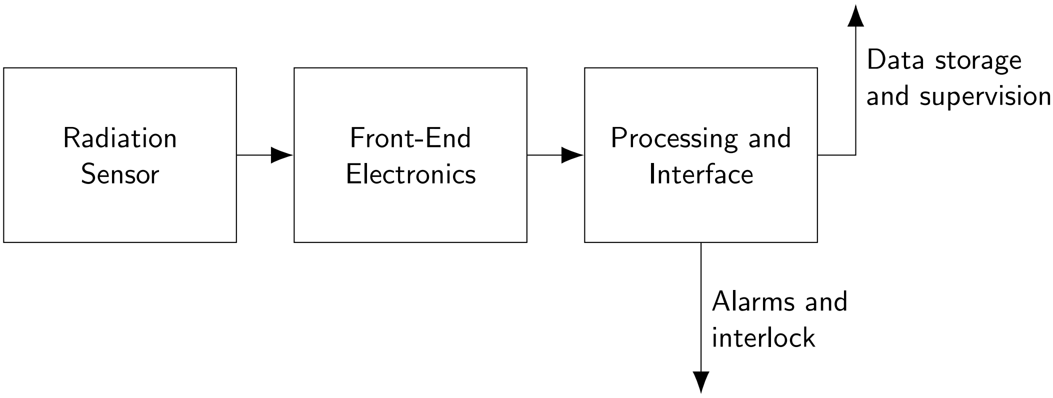

Figure 3: A typical radiation monitoring system

1.4.1 Ionization Chamber

The ionization chamber is one of the oldest and most widely used type of radiation detectors.[7] They work by collecting the charges generated in a gas due to ionizing radiation, by using a strong electric field across electrodes, generated with a biasing voltage V_{bias}. Thus, the produced current on the electrodes is linked to the amount of charges collected, and to the amount of incident ionizing radiation. The gas used, as well as its pressure and geometry can vary between devices. The most common geometric shape and recording method can be found in figure 4.

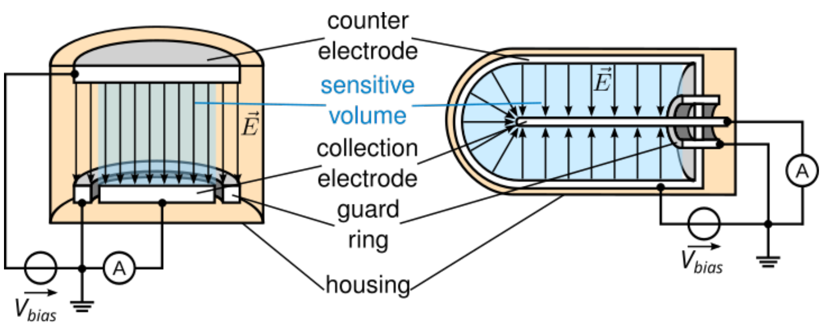

Figure 4: Schematic drawing of the two most common ionization chamber geometries: planar and thimble on the left and right, respectively.[12]

As charge carriers are generated inside of the chamber, positive and negative carriers may encounter each other, equilizing their charge without going to the measurement equipement. This process is called "recombination" and resulting in losses in the current detection. The phenomenon influencing charge recombination are complex and depend if the radiation event can be considered constant (static) or variable (i.e. pulsed). The ionization is considered constant if "no appreciable change of intensity takes place within a time of the order of the transit time of the positive ions through the chamber. This time is usually of the order of milliseconds." [13].

Given a properly designed ionization chamber in normal operation (reasonable biasing voltage, a reasonably intense constant irradiation), recombination may be considered negligible and thus, current generation to be proportional to the dose rate, with a factor determined by the construction of the chamber.

Pulsed regime of an ionization chamber is much more complicated to model, due to the high density of carriers present in the gas during the pulse, making recombination much more likely. Moreover, the behaviour of the chamber may also become dependant on the biasing voltage, resulting in different regions of operation, as depicted in figure 5. The region of interest is the ion saturation, as the total charge collected does not depend (much) on the biasing voltage, thus a amount of resistance on the return path of the charges can be tolerated. It can be noted that an ideal measuring device for pulsed regime would have zero resistance.

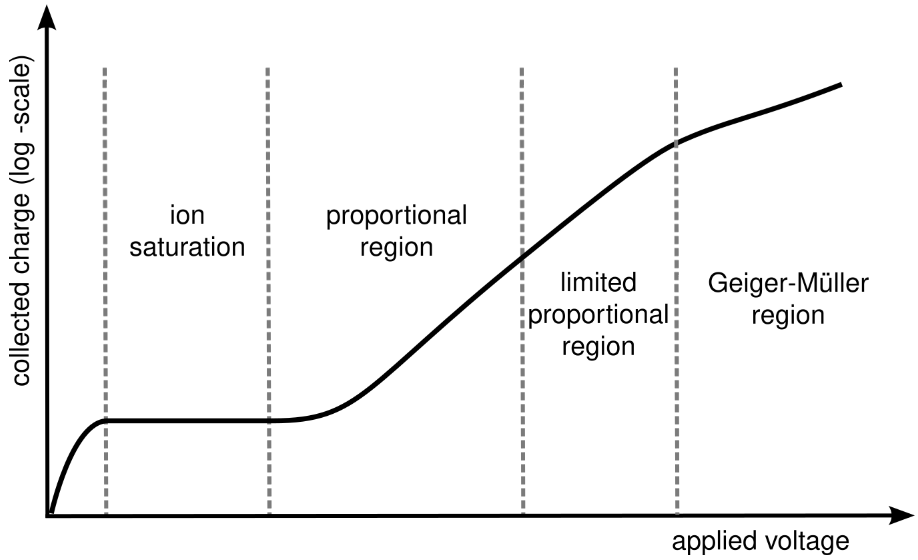

Figure 5: Collected charge over the biasing voltage, for the same pulsed event [12][7]

J. W. Boag investigated the recombination in pulsed ion beams, and later developed an extension to the work with Hochhäuser and Balk[14], which derived an efficiency factor f[2], linking the charge ideally delivered by the ionization chamber to the real charge collected. The behaviour of CERN's ionization chamber in pulsed beam has been evaluated in [15] and has shown that the theory does not apply well to argon-filled chambers, with the proposed explanation being the impossibility to form negative ions in this gas.

The experiments made in this thesis will be performed with one of the most commonly used ionization chamber at CERN, the Centronic's IG5-A20 chamber. This chamber contains $5\,\mathrm{L}$ of argon at $20\ \mathrm{atm}$. It is used for dose rate measurements from $50\,\mathrm{nSv\,h^{-1}}$ to $100\,\mathrm{mSv\,h^{-1}}$, and is usually biased with a voltage of $-1000\,\mathrm{V}$.

A first order approximation of the ionization chamber will be used initially in this thesis, presenting the chamber either as a current source with a constant current source for the static regime or as a Kronecker's delta charge injection in the pulsed regime. Since that as long as the voltage drop over the measuring device is small in front of V_{bias}, no effect from the biasing voltage should be seen on the behaviour of the device, it may be omitted in the diagrams[3]. Due to its geometry and being a 'real' device, the ionization has a certain amount of parasitic capacitance, measured experimentally for the IG5 to be $50\,\mathrm{fF}$.

[2]Sometimes referred in the literature as k_s

[3]or rather 'included' inside the current source

1.4.2 Front-End Electronics

The front-end currently used in CROME uses reset counting, as well as some ADC measurement to increase its resolution. Its block diagram is shown in figure 6. The operational amplifier

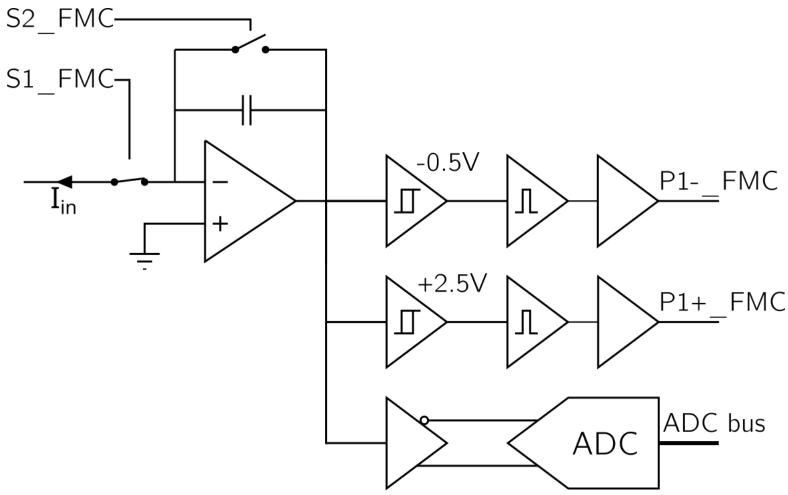

Figure 6: Block Diagram of the Front-End

integrates I_{in}, causing its output to rise. When a certain threshold voltage is reached, the input is briefly disconnected ($S1\_FMC$) while the integrator is reset ($S2\_FMC$), before starting the integration again. Because the voltage at the output of the opamp is at the moment of the reset is equal to the threshold voltage, it is trivial to find how much charge was inside of the feedback capacitor. CROME functions using an interval t_{sample} (usually $100\,\mathrm{ms}$) at which the integrated charge over the cycle is forwarded to the rest of the system. In order to increase the resolution of the integrated charge, the output voltage is read at each end of the cycle and the integrated charge is increased by the corresponding amount. In order to avoid counting the same charge twice, the previous reading is subtracted from the total.

A typical sample measurement is shown in figure 7. If at any point the positive leakage current is higher than the input current, the opamp will start integrating in the other direction, which is why there is a comparator at $-0.5\,\mathrm{V}$.

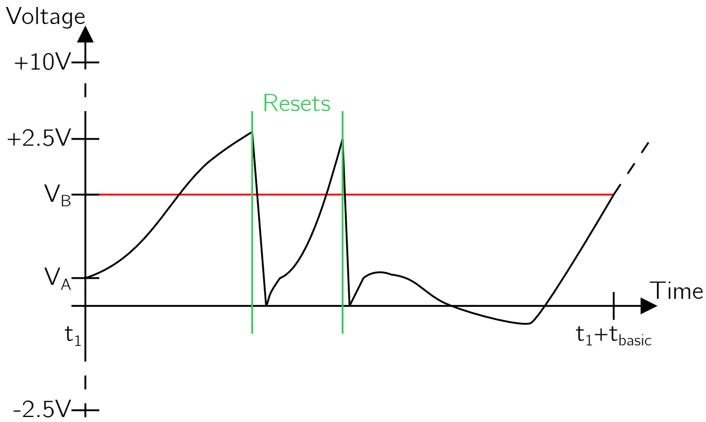

Figure 7: Voltage at the output of the CROME opamp during a sample measurement

It is worth noting that the front-end and subsequently the whole processing unit uses the "raw" voltage sum instead of converting it to a direct representation of the dose or dose rate. This is because the two quantities have a linear relationship, and thus resources can be saved by correcting the parameters used further down the line (safety thresholds,...) instead of using an additional converter block in the design.

1.4.3 Processing and Interface

CROME's processing unit is based on a Zynq SoC, which incorporates:

- The **Programmable Logic (PL)**: FPGA fabric taking care of the safety critical processing. It extracts the average dose rate and total dose over predefined intervals and potentially trigger different signals depending on the configurable safety levels.
- The **Processing System (PS)**: linux-capable ARM cores which interfaces with the supervision. It is not directly part of the data path of safety critical data, however it can influence the processing of the data in the PL by providing parameters such as measurement time, thresholds, averaging method, etc... It also reports data the cloud (REMUS), but it is only used as logging and will not trigger alarms.

Processing Logic As depicted in figure 8, the PL has the following dataflow for the critical data:

1. Interfaces with the front-end. Does a sample measurement of the charge every t_{sample}.
2. Compensate the sample with respect to temperature.
3. Aggregate samples over a specific "MeasurementTime" (MT), expressed in a multiple of t_{sample}.
4. Every MT, check that:
   (a) The average rate does not exceed certain thresholds (with hysteresis). The type of average used for the safety function is selectable.
   (b) The total dose over a certain period does not exceed certain thresholds (with hysteresis). There are two module with different periods.
5. Choose what to do based on the internal safety indicators, external inputs, faults, and configuration. This happens in the "Matrices" block.
6. Propagate decision to the interlock connector and CROME Alarm Unit (CAU).

It is worth noting that there is two external sources that influences the output of the PL: the front-end and the external inputs. The reason behind the usage of external inputs is to add flexibility to the system. For example, one may want to not raise alarms if the doors leading to a particular area are locked.

As the PL needs to be extremely reliable, many techniques are used to ensure proper operation, such as the usage of triplication, ECC, and more.

Processing System As mentioned previously, CROME's PS main goal is the communication to the supervision, so that monitoring data is recorded and the device is configurable by the end user. Because the internet connection deemed too unreliable to rely fully on it, all the local data, including integrated/average dose rates and events such as detected faults or alarm are stored locally. This new historical data is then sent periodically to the supervision. If for some reason the connection was broken, all the data that the supervision lacks is sent. The PS also has the capabilities of sending data in real time, which is very useful for debugging. The communication to the PL is bidirectional done through FIFOs. It is updated every t_{sample}.

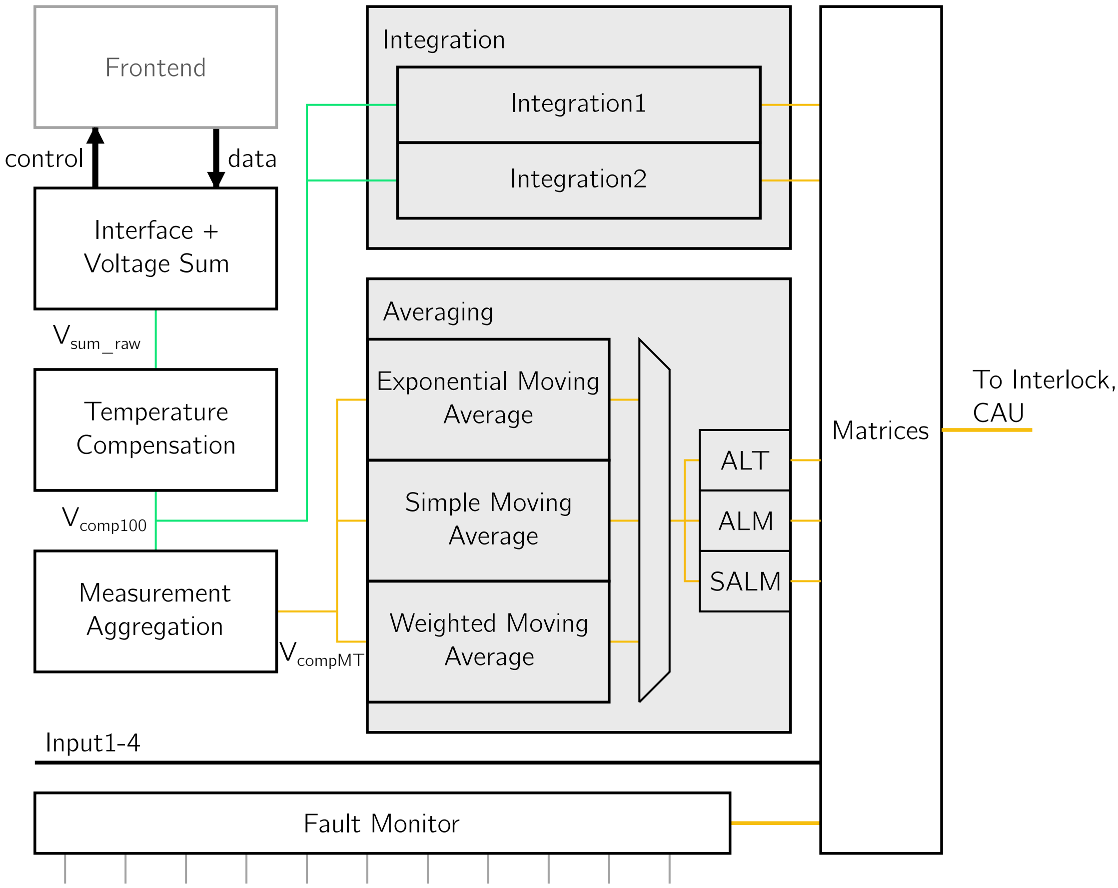

Figure 8: Block Diagram of CROME's PL. The green and orange signals have an update frequency of t_{sample} and $t_{measurement}$, respectively. Not depicted: the communication with the PS.

1.4.4 Functional Requirements for CROME

The "CMPU Technical Specifications" specify requirements concerning different aspects of the device. The main highlights concerning the front-end are:

1. The input current range shall be at least 8 decades: from $-2\,\mathrm{fA}$ to $-250\,\mathrm{nA}$.
2. The device shall be able to measure pulses up to $-500\,\mathrm{nC}$ charges per pulse with an exponential pulse shape of duration of $10\,\mathrm{ms}$ and 75% of the charge in first $2\,\mathrm{ms}$, with maximum repetition frequency of $10\,\mathrm{Hz}$.
3. The real current must be $\pm(1.0\%$ of the reading $+\ 10\,\mathrm{fA})$.

These specifications allow for a single CROME device to be connected to all ionization chambers used at CERN without requiring any modifications. It is worth noting that while the specifications serve as a solid basis for the development of CROME, they are the product of constant discussion between CROME's development team and end-users and thus may be subject to modification.

1.5 Motivation For This Work

The unavailability of commercial products which would demonstrate the required dynamic range was the driving force for undertaking in-house development of radiation monitoring systems. The front-end of legacy systems and the latest generation of installed radiation monitors are all based on discrete components. The management of such a complex system with thousands of components is a herculean task and bears the unavoidable risk of obsolescence of the components. Hence, an application specific integrated circuit (ASIC) development program was initiated at the Instrumentation Laboratory (IL).

The initial effort started in the form of the UTOPIA series[16]. While the potential of the second version of the ASIC was clear, several field test showed the need to increase its performance. Unfortunately, a direct upgrade of the chip was not feasible, due to the unavailability of the node size ($350\,\mathrm{nm}$) used in its design. As no previous work described the suitability of smaller, more available nodes for this design, research had to be made to evaluate the practicality of changing node size. The result of the study yielded a new series of ASICs, Accurate. Extensive characterization of the latest ASIC, Accurate 2 has been made, showing excellent performance in static regime over the full specified range and beyond, but lacking in pulsed regime. [17]

This thesis starts with the modelling of Accurate 2A, both in static and pulsed regime, and establishes a direction for potential improvements, the main one being the increase in input capacitance of the chip. From this results, chapter 3 follows, showing trade-offs and challenges of adding components on the input path, as well as present different input circuitry topologies, containing one or two ASICs. Chapter 4 presents the design of the prototype boards, which implement the increased input capacitance improvement. Chapter 5 describes the modification done to integrate Accurate 2A, including front-ends using multiple ASICs.

The resulting device was then tested at multiple facilities, as explained in chapter 6. Calibration and testing of the linear regime was made at IL's laboratory, using a current source. Practical measurements of constant irradiation was performed at CERN's Calibration Laboratory. Pulsed regime was then characterized at IRA, using train of pulses and produced unexpected results which questions previous assumptions about the recovery time needed for the IG5 ionization chamber after a pulse event to reach internal steady state. In addition, first order approximation of the ionization chamber in pulsed regime were evaluated, using practical measurements. Good performance improvements in pulsed regime due to the increased capacitance was strongly suggested. The impact on the linear regime operation was small, despite imperfection of real world components. The conclusion of the thesis and direction for further improvements is presented in the final chapter.

2 The Accurate 2A ASIC

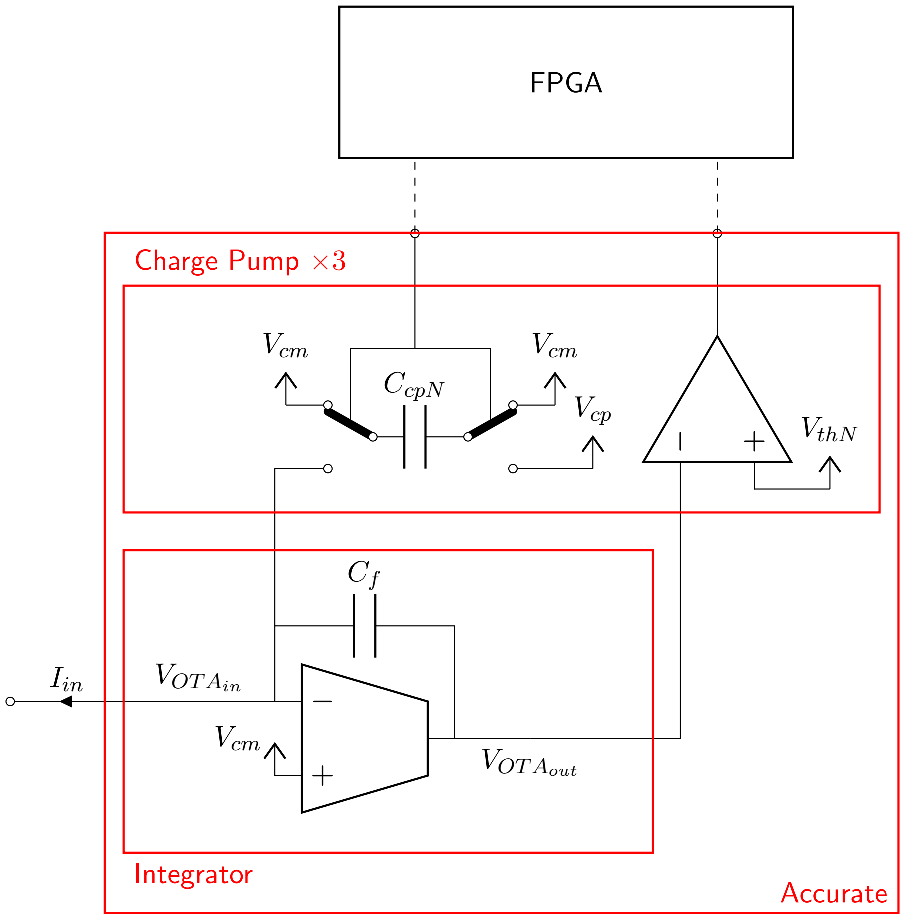

Figure 9: Simplified diagram of Accurate. Not depicted: *cap_clk*

A simplified block diagram of Accurate is shown in figure 9. The device is an OTA-based charge integrator and works using a charge balancing method.

This means that, as the current I_{in} is flowing, the charges given by the OTA accumulate in the feedback capacitor C_f, thus the output voltage of the OTA, $V_{OTA_{out}}$ increases. Once this voltage reaches a certain threshold value V_{th_N}, the FPGA triggers the activation of the corresponding Nth charge pump by connecting its capacitor C_{cpN}, initially discharged, between V_{cp} and the $V_{OTA_{in}}$.

With an ideal OTA, the charge given to the system Q_{dec_N} is exactly known:

$$Q_{dec_N} = C_{cp_N}(V_{cp} - V_{cm}) \tag{3}$$

Since Q_{dec_N} is well know, it is then easy to find the average current by dividing it by the time. In CROME, this will be done by counting the number of activation over t_{sample}, and report the total charge divided by that period.

Figure 10 show the behaviour of $V_{OTA_{out}}$ w.r.t the time. It can be noted that the current suddenly increases in the middle of the graph, as the activation of the charge pump gets higher in frequency.

Two main operation regimes can be noted:

- Non-Saturating: The input current is low and/or smooth enough for the output stage of the OTA to not saturate, thus $V_{OTA_{in}} \approx V_{cm}$.

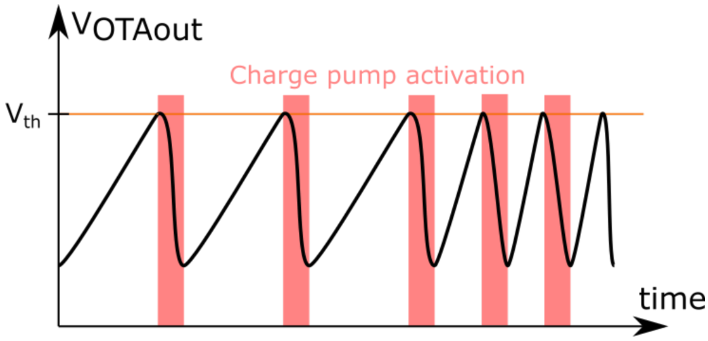

Figure 10: $V_{OTA_{out}}$ versus time for an arbitrary input current

- Saturating: Due to a temporary spike in current, the output stage of the OTA saturates, thus $V_{OTA_{in}} \neq V_{cm}$. This in turns lead to errors in the current reporting, as the charge pumps will not deliver a constant amount of charge per activation anymore.

As both of these operation regimes are quite different in their behaviour, different approaches for modelling them will be taken.

In this section will be studied the behaviour of Accurate, taking into account the parasitic capacitance C_{in} at its output node, the finite transconductance of the OTA g_m, as well as the amount of time the charge pumps are connected to $V_{OTA_{in}}$ per activation, T_{co}.

This can be used to approximate the behaviour of the device when connected without any additional discrete components connected to its input, apart from a (lumped-C modelled) cable connected to an ionization chamber. Because the capacitance of the cable is typically much higher than the capacitance of the capacitance of the ionization chamber ($50\,\text{fF}$), C_{ion} may be neglected. This configuration is shown in figure 11.

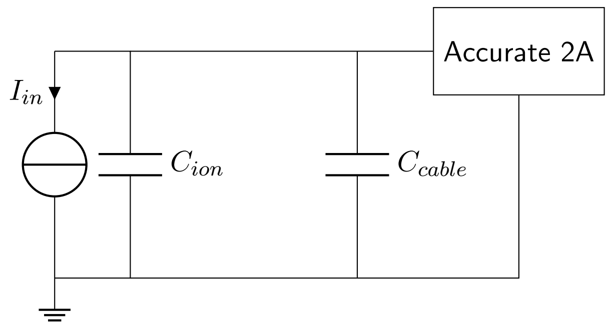

Figure 11: Block diagram of bare Accurate

One can note that the biasing voltage source is missing from this diagram. It is a deliberate choice because as long the voltage drop on Accurate is small in front of V_{bias}, its effect on the creation of ions is constant. Moreover the offset error of the OTA will not be taken into account, as it has no influence in any of the models in this section, since there is resistance to ground considered.[4]

In this section or the following, the numerical value of any non-explicitly defined variable can be found in appendix A. Moreover, the set of assumptions for each model will allow proper modelling with a single charge pump. To model higher currents, where two charge pumps are active, C_{cp} is simply increase by the amount of capacitance of the next charge pump.

[4] One can substitute V_{cm} to $V_{cm} + \epsilon_{OTA}$ to obtain the equations with the OTA offset.

2.1 Non-Saturating regime

In this regime, the dynamic behaviour of the device can be described by two alternating circuit configurations. In the first configuration, named Current Integration and lasting T_{ci}, the charge pump is disconnected and $V_{OTA_{out}}$ is steadily increasing. Since at the start of this configuration, the device may not be in steady state, it is important to consider its transient behaviour.

When the output voltage reaches a certain threshold, the corresponding charge pump is connected to the system during an set time T_{co}. This configuration is called "Charge Pump Connection".

For a constant input current I_{in} and a system in steady state, the detected current I_{dec} can be found using the following:

$$I_{dec} = \frac{C_{cp}(V_{cp} - V_{cm})}{T_{co} + T_{ci}} \tag{4}$$

It is worth noting that because there is a succession of different stages, the steady state of the whole system is not necessarily the same as the steady state of one of its components. Thus, in order to accurately find I_{dec}, one must infinitely iterate over the stages to find the correct initial values.

The assumptions used here are:

- The charge pump is always in steady state before being connected to the current input.
- There is no leakage from the input to ground.
- Resistance between the ionization chamber and Accurate is negligible.
- The charge pump activation are all equally spaced in time (i.e. no double triggering of the charge pumps).
- The input current is constant.
- Apart from its transconductance g_m, the OTA is ideal.

2.1.1 Current Integration

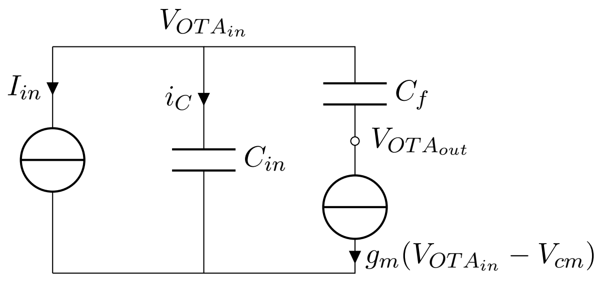

Figure 12: Block diagram of bare Accurate in the current integration regime

The diagram used for the derivations is shown in figure 12. Using Kirchoff's law and solving the differential equation for an initial value of $V_{OTA_{in}}(0) = V_{OTA_{in}}(\infty) + \epsilon$, ϵ being an arbitrary offset, the following is obtained:

$$I_{in} + i_C + i_{OTA} = 0 \tag{5}$$
$$I_{in} + C_{in}\dot{V}_{OTA_{in}} + g_m(V_{OTA_{in}} - V_{cm}) = 0 \tag{6}$$
$$V_{OTA_{in}}(t) = V_{cm} - \frac{I_{in}}{g_m} + \epsilon e^{-\frac{t}{\tau_{sys}}}, \text{ with } \tau_{sys} = C_{in}/g_m \tag{7}$$

It can be seen that the input capacitance has a direct effect on the speed at which the OTA is able to respond to a change at its input. For an input capacitance of $\sim 1\,\mathrm{nF}$, as can be easily obtained with a cable that is a few meters long, $\tau_{sys} \approx 300\,\mathrm{ns}$, which is not negligible compared to the T_{co} of $70\,\mathrm{ns}$ used in previous works.

In addition, one can note that the steady-state voltage is not precisely at V_{cm}. Thus, depending on T_{ci}, τ_{sys} and I_{in}, the charge pumps will give slightly more charge than expected. This error goes always in the same direction (more charge given), as it is necessary for $V_{OTA_{in}}$ to go below V_{cm} in order to integrate in the other way and thus avoid negative saturation.

It can be noted that this effect is relatively small as the maximum difference in voltage for $I_{in} = 10\,\mu\mathrm{A}$ is $3\,\mathrm{mV}$, thus causing at worst an error of less than half a percent.

2.1.2 Charge Pump Connection

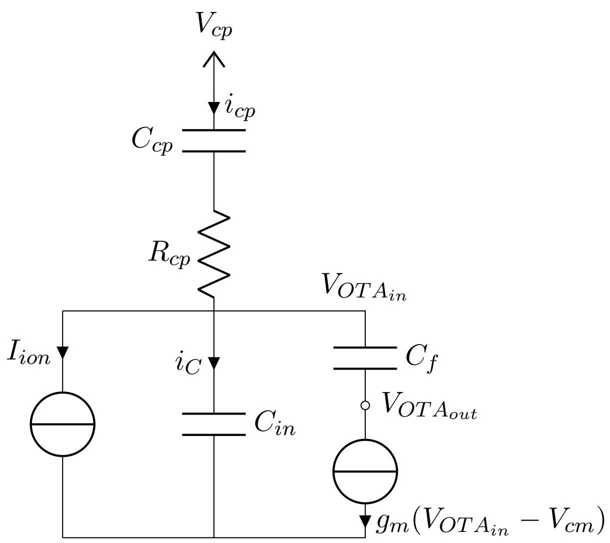

Figure 13: Block diagram of bare Accurate in the charge pump regime

Using Kirchoff's law and a derivative term, one can find:

$$I_{in} + \dot{V}_{OTA_{in}}C_{in} + g_m(V_{OTA_{in}} - V_{cm}) = i_{cp} \tag{8}$$
$$-\dot{V}_{OTA_{in}} = \frac{1}{C_{cp}}i_{cp} + R_{cp}\dot{i}_{cp} \tag{9}$$

Which is a system of first order differential equations. Let us define:

$$\vec{x} = \begin{pmatrix} V_{OTA_{in}}(t) \\ i_{cp}(t) \end{pmatrix} \tag{10}$$

Equation 8 and 9 can then be expressed as:

$$\dot{\vec{x}} = A\vec{x} + \vec{g} \tag{11}$$

The homogeneous solution is in the form of[18]:

$$\vec{x}(t) = k_1\vec{\eta_1}e^{\frac{-t}{\gamma_1}} + k_2\vec{\eta_2}e^{\frac{-t}{\gamma_2}} \tag{12}$$

With η_n and λ_n the eigenvector and corresponding eigenvalue, respectively.

The particular solution, $\vec{x_p}$ is found using:

$$\vec{x_p} = X\int X^{-1}\vec{g}dt \tag{13}$$

With X the column matrix of linearly independent solution to the system. It is then found:

$$\vec{x_p} = \begin{pmatrix} V_{cm} - \frac{I_{in}}{g_m} \\ 0 \end{pmatrix} \tag{14}$$

Which is in adequation with what was found for the current integration regime.

The initial value is defined as:

$$\vec{x}(0) = \begin{pmatrix} V_{cm} - \frac{I_{in}}{g_m} + \epsilon \\ \frac{V_{cm} - \frac{I_{in}}{g_m} + \epsilon}{R_{cp}} \end{pmatrix} \tag{15}$$

Solving the system to find the value k_1 and k_2 yields a solution in the form of:

$$k_1 = A_1\epsilon + B_1 \tag{16}$$

$$k_2 = A_2\epsilon + B_2 \tag{17}$$

A_n and B_n being constant terms w.r.t epsilon depending on γ_n, I_{in}, V_{cp} and the different values of the components used.

Due to the number of terms' explosion when finding the eigenvalues, sympy, a python symbolic solver was used for the derivations. Because of this the general solution will not be substituted in this document with the original variables. Details can be found in the appendix B.

It is however important to note the behaviour of the solution. One of the exponential will describe rise of $V_{OTA_{in}}$ due to the effect of the charge pump and the other will show the fall in $V_{OTA_{in}}$ due to the transconductance of the OTA.

Depending on the numerical value of T_{co}, and γ_n, two main behaviour can be seen:

1. The integration effect by the OTA takes is shorter than the connection time, which results in the perfect scenario where steady state is reached before the disconnection of the charge pump and thus, no charges are left inside of them. Thus is no negative impact on the accuracy.

2. The integration effect by the OTA is much longer than the connection time, which results in the charges being divided between the input capacitance and the charge pump's capacitance, thus leaving some charges inside C_{cp} at disconnection. There *is* an impact on accuracy, depending on the size of C_{in}.

It is also worth noting that the input capacitance affects both the speed of integration of the OTA and the amount of charges that may remain in the charge pump at the time of disconnection. There must thus exist an input capacitance value that if big enough for slowing the system down sufficiently for the steady state to not be reached, but is not big enough for the charges remaining in the feedback capacitor to be negligible. This would not be an issue if the input current effect during the charge pump regime could always be neglected, as the error would simply be a relative offset and thus easy to compensate for, but it may not always be the case.

2.1.3 Finding the Steady State

Let us recall the results found for each configuration, and assign denote the regime using $^{(1)}$ and $^{(2)}$:

$$
\begin{aligned}
V_{OTA_{in}}^{(1)}(t) &= V_{cm} - \frac{I_{in}}{g_m} && + \epsilon e^{-\frac{t}{\tau_{sys}}} \\
\begin{pmatrix} V_{OTA_{in}}^{(2)}(t) \\ i_{cp}^{(2)}(t) \end{pmatrix} &= \begin{pmatrix} V_{cm} - \frac{I_{in}}{g_m} \\ 0 \end{pmatrix} && + k_1 \vec{\eta_1} e^{-\lambda_1 t} + k_2 \vec{\eta_2} e^{-\lambda_2 t}
\end{aligned}
$$

Since we assumed I_{in} constant and regular activation in time, T_{co} and T_{ci} must also be constant at steady state.

Let us find the offset at the end of the regime and redefine the k terms:

$$
\begin{aligned}
\epsilon_n^{(1)} &= \epsilon_{n-1}^{(2)} e^{-\frac{T_{ci}}{\tau_{sys}}} \\
\epsilon_n^{(2)} &= (\epsilon_n^{(1)} A_1 + B_1)\eta_{11} e^{-\lambda_1 T_{co}} + (\epsilon_n^{(1)} A_2 + B_2)\eta_{21} e^{-\lambda_2 T_{co}} \\
\epsilon_n^{(2)} &= \epsilon_n^{(1)} (A_1 \eta_{11} e^{-\lambda_1 T_{co}} + A_2 \eta_{21} e^{-\lambda_2 T_{co}}) + (B_1 \eta_{11} e^{-\lambda_1 T_{co}} + B_2 \eta_{21} e^{-\lambda_2 T_{co}})
\end{aligned}
$$

A change of variable can be made to simplify the above equations:

$$U = e^{-\frac{T_{ci}}{\tau_{sys}}} \tag{18}$$
$$S = (A_1 \eta_{11} e^{-\lambda_1 T_{co}} + A_2 \eta_{21} e^{-\lambda_2 T_{co}}) \tag{19}$$
$$Q = (B_1 \eta_{11} e^{-\lambda_1 T_{co}} e^{-\lambda_1 T_{co}} + B_2 \eta_{21} e^{-\lambda_2 T_{co}}) \tag{20}$$
$$\tag{21}$$

Which yields:

$$\epsilon_n^{(1)} = \epsilon_{n-1}^{(2)} U \tag{22}$$
$$\epsilon_n^{(2)} = \epsilon_n^{(1)} S + Q \tag{23}$$
$$\tag{24}$$

It can then be derived that:

$$\epsilon_n^{(1)} = UQ \sum_{i=0}^{n} (US)^i \tag{25}$$
$$\epsilon_\infty^{(1)} = \frac{UQ}{1 - US} \text{ with } |US| < 1 \tag{26}$$

$\epsilon_\infty^{(1)}$ will be used as the starting point of the simulations done in the next section.

2.1.4 Values of Interest and Theoretical Results

The most interesting values describing our device are its accuracy and its noise tolerance, as well as how they are affected by C_{in} and T_{co}, the main parameters not intrinsic to the ASIC.

For both these terms, one needs to find the value of T_{ci} for a given I_{in}. This can be done by setting the total integrated charge over a full cycle of the device equal to zero, which is the situation where the output voltage of the OTA stays within the same range each cycle (steady state):

$$Q_{OTA}(T_{ci}+T_{co}) = g_m \int_0^{T_{ci}+T_{co}} \left(V_{OTA_{in}(t)} - V_{cm}\right) dt = 0 \tag{27}$$

Because T_{ci} affects both the offsets $\epsilon^{(n)}$ and the OTA's response, finding its value is non-trivial to find and thus numerical approximation will be used.

The relative error of the device is then defined as $I_{dec}/I_{in} - 1$, as show in figure 14.

The behaviour described in section 2.1.2, where the input capacitance can be neither low nor high enough and thus maximize the error can be seen, with the worst value being affected by both T_{co} and C_{cp}. From these graphs, on can also wonder why different charge pumps are used. The main reason for that is the increase in the maximum deliverable current, while keeping the low current resolution acceptable.

It is also worth mentioning the effect of T_{co}. The smaller its value, the bigger the relative error at low C_{in} values. This is comes from the fact that the OTA does not have time to stabilize the input during T_{co} and thus a significant portion of the charge is split between C_{cp} and C_{in}. This also explain why large C_{in} values are largely unaffected by this behaviour, as the bigger it is, the less charges are in the charge pump at disconnection in capacitor ladder scenarios.

The fact that the relative error is constant over the whole range indicates that it is possible to correct the reading through a calibration. It may however be a bad idea, as the precise amount of input capacitance is not known in advance (the ASIC could be connected to an ionization chamber through a long cable, or directly to it). However, in order to guarantee results, one may deliberately put a certain amount of capacitance ($\sim 10\,\mathrm{nF}$) at the input, so that the system may not reach the worst case.

Let us now discuss noise tolerance. The tolerance of our system to noise can be measured by the effect that the charge pump discharge has on $V_{OTA_{out}}$, both in amplitude and in time. The bigger the amplitude and the smaller the time to reach the maximum amplitude, the less spurious activation of the charge pump are likely to happen after their current compensating activation.

These spurious activation may impact the performance of the system in two main ways:

1. Loss of resolution in the low currents range: if the time taken to see a significant effect on the charge pump is longer than their cycle time, they will always be triggered in bunches. This causes the system to lose time and current resolution because the system acts as if we injected a single time a bigger charge than the actual charge pump and cause the system to wait longer for the input current to compensate this injection.

2. Loss of accuracy: in extreme cases, consecutive spurious activation may raise $V_{OTA_{in}}$ which will in turn lead to an underestimation of the current. More work is needed to evaluate this effect quantitatively.

Figure 15 show the maximum change in voltage at the output of the OTA due to a single activation of the charge pump and after how much time that maximum is reached.

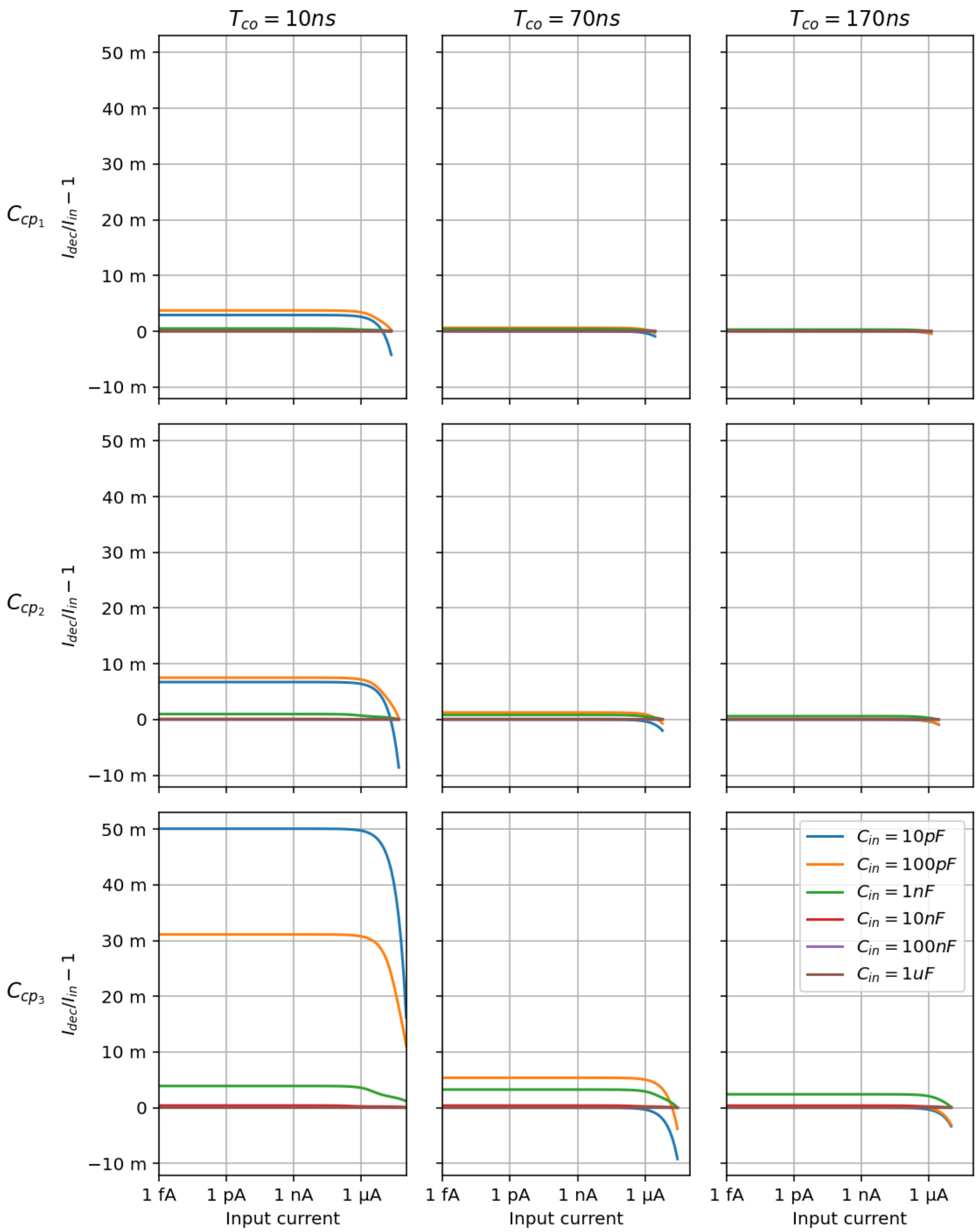

Figure 14: Relative error of bareAccurate for each charge pump

It is also interesting to note, that because of the amplitude of the output voltage may vary depending on I_{in}, as well as the increased noise sensitivity, and delay to see the effect of the charge pump at the output, measurement of the current using a direct slope method does not seem like a practical combination with charge balancing when a significant amount of input capacitance is present in addition to a high input current.

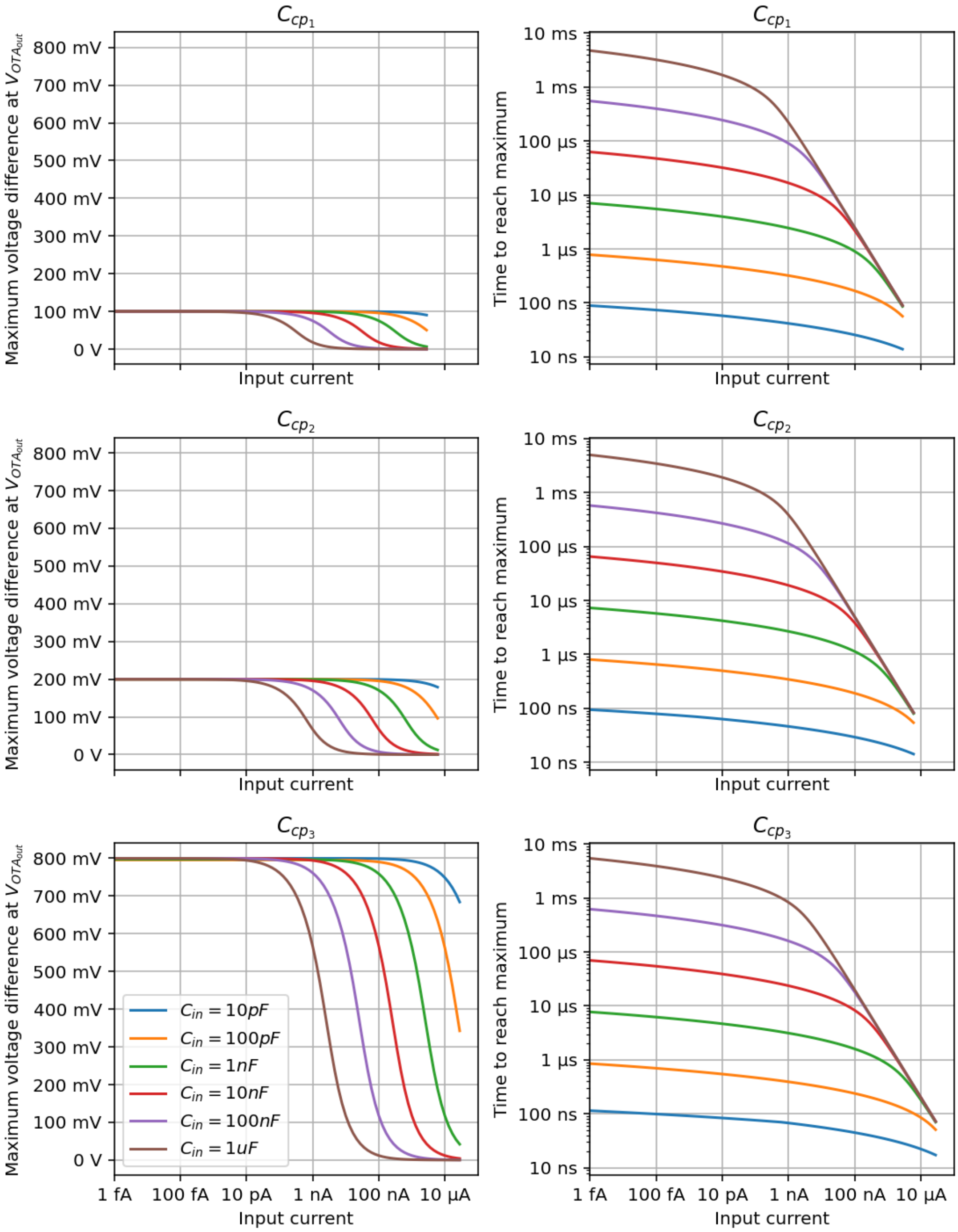

Figure 15: Effect of C_{in} on the output voltage of the OTA

.

2.2 Saturating Regime

The saturating (or pulsed) regime of Accurate may seem like highly non-linear: the OTA saturates, the charge pump discharges periodically : the systems goes through different phases during an event. It is however possible to make a linear model out of it using the following approximations:

The OTA is immediately saturating. Considering that the OTA will saturate in $t = C_{cp_3}(V_{cp} - V_{cm})/I_{OTA_{max}} =\sim 50\,\text{ns}$, this is reasonable.

The charge pump is considered only using its average current, which is composed of a constant term and an additional error term with a linear dependency on the difference between $V_{OTA_{in}}$ and V_{cm}. For this, the time constant $\tau_{cp} = R_{cp}C_{cp}$ [5] must be much smaller than Accurate's cycle ($\tau_{cp} \approx 1\,\text{ns} << T_{cycle} = 150\,\text{ns}$). Then, the average current delivered over a full cycle is given by:

$$I_{cp} = Q_{cp}/T_{cycle} = \frac{C_{cp}}{T_{cycle}} \frac{C_{in} + C_f}{C_{in} + C_f + C_{cp}} \cdot (V_{cp} - V_{in_{OTA}}) \tag{28}$$

$$= \frac{C_{cp}}{T_{cycle}} \frac{C_{in} + C_f}{C_{in} + C_f + C_{cp}} \cdot (V_{cp} - V_{cm} - V_{err}) \tag{29}$$

$$= I_0 - \alpha V_{err} \tag{30}$$

The loss of charges happens only during the saturation of the OTA. This allows us to stop the simulation when the input voltage reaches V_{cm}, and to get the detected charges by subtracting the total charge given to the system by the charge losses. Given the results of the previous section, this is reasonable for an Accurate which has correct parameters.

The ESD diodes present at the input of the ASIC are assumed to stay inactive. This is true only if $V_{OTA_{in}}$ stays within a reasonable margin ($\sim 0\,\text{V} \to \sim 3\,\text{V}$) and will need to be checked.

Moreover, in order to ease the computation and without loss of generality, V_{cm} will be considered equal to zero. If one wants to extract the real voltage from the values that will follow, the true V_{cm} (usually $1.5\,\text{V}$) must be added.

Finally the current pulse shape will be assumed to be a Kronecker's delta, though this will be discussed later on.

2.2.1 LTI Modelling of Accurate in the Saturating Regime

Figure 16 shows the equivalent circuit of the Accurate in saturating regime.

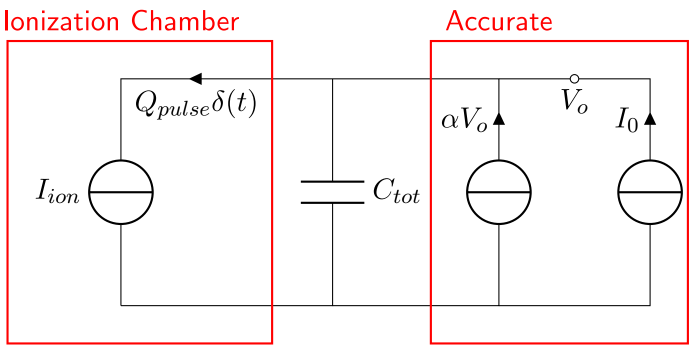

Figure 16: Diagram of Accurate in saturating regime

The term the most interesting to us is the unaccounted excess of charges given to the

[5] The R_{cp} value is a rough estimate considering the resistance of the output transistors in triode regime and the resistance of the voltage source

system $Q_{excess} = \int_{t_0}^{t_{end}} \alpha V_o dt$. The following block diagram is obtained, with which any linear components connected to the input can be modelled:

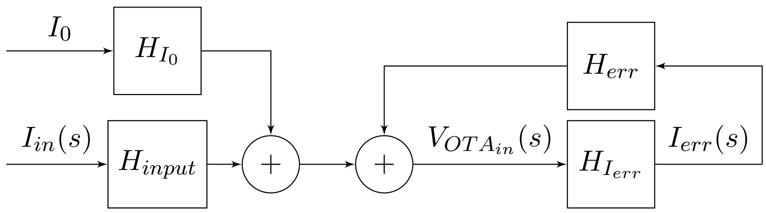

Figure 17: LTI modelling of Accurate in saturating regime

We obtain the following for the transfer functions:

$$\begin{aligned} H_{I_0}(s) &= Z_{tot} \\ H_{input}(s) &= Z_{in} \\ H_{I_{err}} &= -\alpha \\ H_{err}(s) &= Z_{tot} \\ I_0 &= \alpha \cdot (V_{cp} - V_{cm}) \\ \alpha &= \frac{C_{cp}}{T_{cycle}} \frac{C_{in} + C_f}{C_{in} + C_f + C_{cp}} \end{aligned}$$

Z_{tot} being the total equivalent impedance seen from the input of the OTA and Z_{in} the transfer impedance from the output of the ionization chamber to the input of the OTA. In this instance, $Z_{in} = Z_{tot} = 1/(C_{tot}s)$.

For the total system, we have:

$$\begin{aligned} I_{err}(s) &= (I_{ion}(s)H_{in}(s) + H_{I_0}(s)) \frac{-\alpha}{1 + \alpha H_{err}(s)} \\ Q_{err}(s) &= I_{err}(s) \cdot \frac{1}{s} \\ V_{OTA_{in}}(s) &= (I_{ion}(s)H_{in}(s) + H_{I_0}(s)) \frac{1}{1 + \alpha H_{err}(s)} \end{aligned}$$

Using this, it is possible to model the pulsed response of our system for any current input, provided that our requirements are still met.

2.2.2 Theoretical Results

Figure shows the detected charges per pulse with two different input current shapes. The following observations can be made:

- The bigger the input capacitance, the better the charge collection.
- The shape of the input can have a significant effect for low input capacitance. For high input capacitance ($> 100\,\mathrm{nF}$), this effect is negligible.
- The worst case scenario is the Kronecker's delta type of pulses, as it is the one causing the biggest offset at $V_{OTA_{in}}$.

Because of the last two points, the delta discharge will be used for comparing devices, but other types of input shape could be used to explain real-world observations.

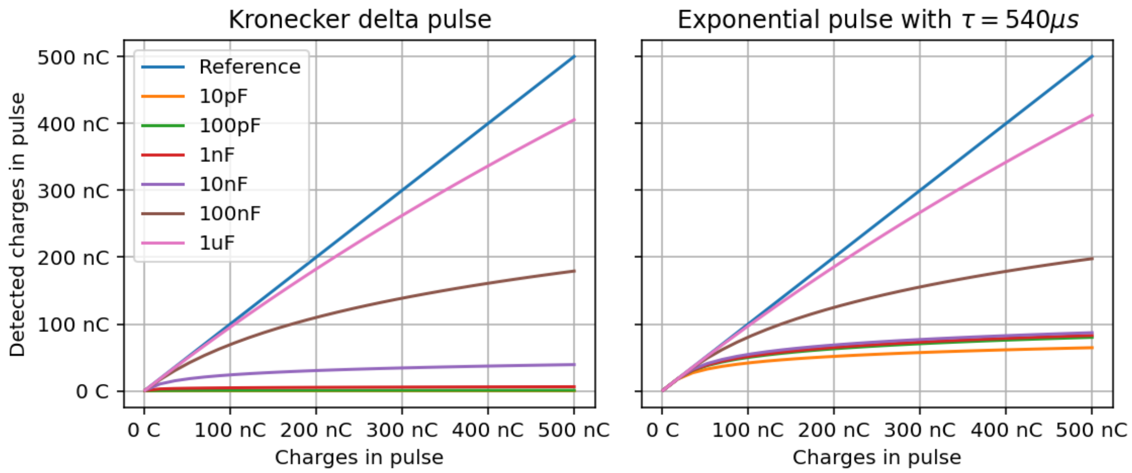

Figure 18: Detected charges per pulse vs total charges per pulse

Note that an additional phenomenon may happen at the end of the saturation of the OTA: as described in section 2.1.4, there exists some delay between events at the input and events at the output of the OTA. Depending on C_{in}, g_m and V_{th} chosen, the charge pumps will overshoot by a constant amount at the end of saturation because even though $V_{OTA_{in}}$ has reached V_{cm}, its effect is not yet seen by the comparators. This may lead to negative saturation of the OTA and a relatively long recovery time after a pulse depending on I_{in}, because Accurate can only add charges to system, not remove them.

Finally, figure 19 describes the maximum voltage drop at the input of the OTA. For the kronecker delta discharge, almost all datapoints reach unreasonable results. Despite out model being simplistic, as there is *some* resistance along path that mitigates a little bit the voltage drop, it is more than likely that the ESD diodes activate to prevent destruction of the device for this type of pulse.

Moreover, wee see that the diodes are likely to trigger even for exponential pulse with a τ in the hundreds of micro seconds. Because there is no clear specification from TSMC concerning the behaviour of the diodes and that the ionization chamber's response is not fully defined, it is hard to draw definitive conclusions concerning their effect on the operation of Accurate.

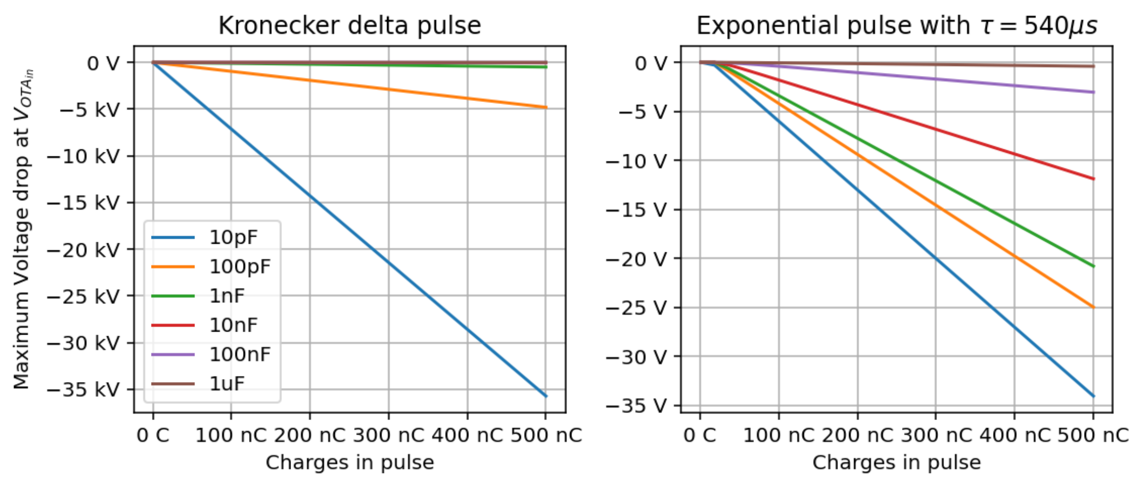

Figure 19: Theoretical maximum voltage drop at the input of the OTA

3 Improving on Accurate 2A

As seen in the previous section, external parameters on the input path, such as the input capacitance have an effect on the behaviour of the device, both in linear and pulsed regime. Here will be explored different configurations of components put on the input path, as well as using multiple ASICs in the hope of improving the pulsed accuracy, while preserving the linear accuracy.

Because the main issue seen in saturating regime is the voltage drop at $V_{OTA_{in}}$, increased input capacitance and low pass filters seem the most promising.

3.1 Imperfection of Real Components

While the integrating OTA structure of our system makes give our system good tolerances on noise and non linear behaviour of external components (such as capacitor value changing w.r.t the input current), one must be careful with the leakage current. For this, the capacitor series "C0G Dielectric, 10 – 250 VDC (Commercial Grade)" from Kemet have been selected for their availability, price, and insulation resistance of $1000\,\mathrm{M\Omega}\,\mu\mathrm{F}$ with an upper limit limit of $100\,\mathrm{G\Omega}$. This means that a smaller value of capacitance increases the insulation resistance until a capacitance of $10\,\mathrm{nF}$ and afterwards stay constant. Moreover all capacitors will be connected between the output path and a voltage source at V_{cm}, in order to limit the static current loss.

If needed, more expensive and harder to source components could be used, such as Murata's Silicon capacitors ($100\,\mathrm{G\Omega}$ for capacitors from $47\,\mathrm{pF}$ to $3.3\,\mu\mathrm{F}$ for HSSC SMD series), Cornell Dubilier's mica capacitors ($100\,\mathrm{G\Omega}$ for capacitors from $47\,\mathrm{pF}$ to $10\,\mathrm{nF}$ for CMD through hole series). RF/Thin film capacitors could also be used for a less flexible improvement ($100\,\mathrm{G\Omega}$ for $100\,\mathrm{nF}$ capacitors of reference ATC 530L). It however seems that there is no capacitor on the market with an advertised insulation resistance higher than $100\,\mathrm{G\Omega}$ suited for our design.

Moreover, depending on the capacitance needed and its location, it may be possible to include a tailored, custom-made capacitor directly inside of the ASIC's design.

3.2 Single Capacitor

As seen previously, increased input capacitance can lead to improved behaviour in pulsed regime. Here will be explored the theoretic behaviour of the system with the added component, taking into account its insulation resistance as well as the possible miss-match between V_{cm} set by Accurate and the guard voltage to which the capacitor is connected to. The DACs used later on in the implementation of this system may have up to 0.4 LSB difference between them, meaning a maximum difference of $\sim 300\,\mu\mathrm{V}$. The offset error of Accurate is not known at this time, but assumed to be significantly lower than the DAC's error. The topology of the ASIC in addition to and additional capacitor will be named capAccurate.

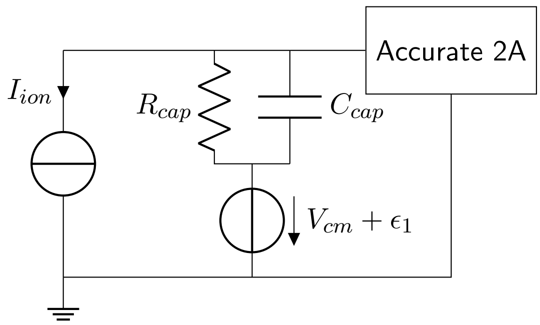

Figure 20: Block diagram of Cap Accurate

3.2.1 Non-Saturating Regime

Using the same approach used in section 2.1, the model of the system can be obtained. The computation's results are detailed in appendix C and appendix D. The most interesting numerical result is the new steady state value of $V_{OTA_{in}}$ for both the current integration and charge pump connection, which is:

$$V_{OTA_{in}\infty} = V_{cm} + \frac{-I_{in} + \epsilon_1/R_{cap}}{g_m + 1/R_{cap}} \tag{31}$$

$$\approx V_{cm} - \frac{I_{in}}{g_m} + \frac{\epsilon_1}{R_{cap}g_m} \tag{32}$$

From that, it can be noted that the effect of the leakage and input current are indistinguishable from each other in steady state.

Using the full model, the theoretic accuracy of capAccurate is found and shown in figure 21. We see excellent linearity over $1\,\mathrm{pA}$ for all cases, but below that results are highly dependent on ϵ_1 and R_{cap} (notice how all of the curves below $100\,\mathrm{nF}$ are bunched together, because of their same insulation resistance of $100\,\mathrm{G\Omega}$). It is also interesting to see that since the leakage current dominates, the effect of the charge pump's capacitance is negligible. Moreover, results show that there is no significant leakage due to dynamic changes in There may be a dynamic effect the leakage, as it depends on $V_{OTA_{in}}$, but results show that it is negligible for practical purposes.

Moreover, it is interesting to see the behaviour at the limit of the graph, which are more easily seen in figure 22. This show that a negative leakage is much more desirable than a positive one, as it is possible to cancel it out the former, while the latter gives us no possibility of that.

Since the results concerning noise tolerance are extremely similar to bareAccurate, the corresponding graph for capAccurate will be omitted.

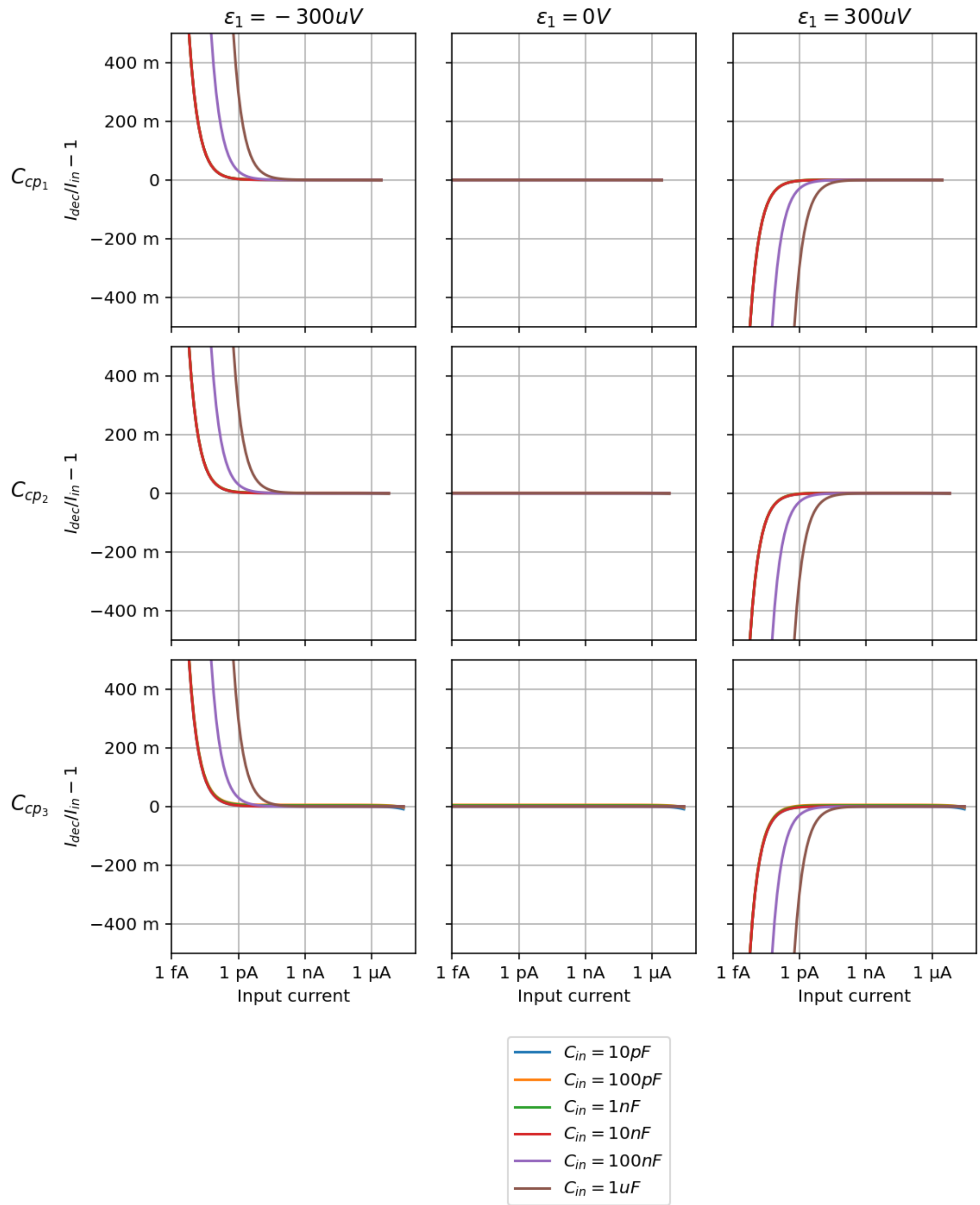

Figure 21: Relative error of capAccurate for each charge pump and worst V_{cm} offsets

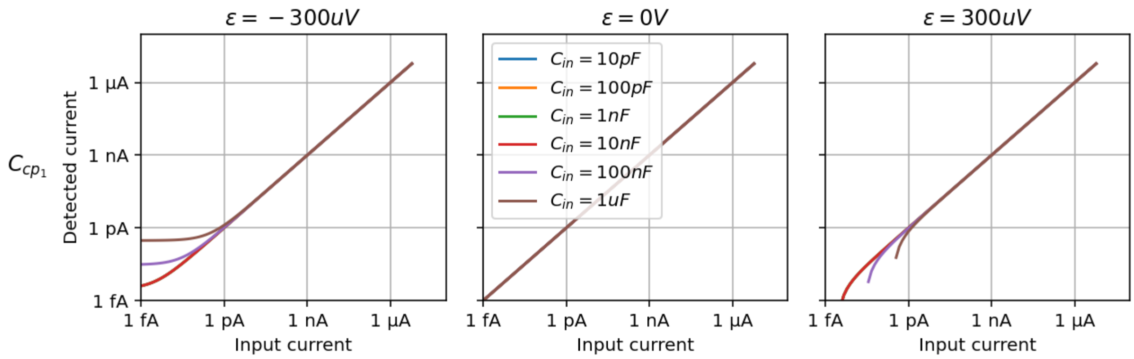

Figure 22: Detected current versus input current

3.2.2 Saturating Regime

Using the same model than bareAccurate, but taking into account the added resistive path, we obtain:

$$
\begin{aligned}
H_{I_0}(s) &= Z_{tot} \\
H_{input} &= Z_{tot} \\
H_{I_{err}} &= -(1/R_{cap} + \alpha) \\
H_{err}(s) &= Z_{tot} \\
I_0 &= \alpha \cdot (V_{cp} - V_{cm}) \\
\alpha &= \frac{C_{cp}}{T_{cycle}} \frac{C_{in} + C_f}{C_{in} + C_f + C_{cp}} \\
Z_{tot} &= \frac{R_{cap}}{C_{in} R_{cap} s + 1}
\end{aligned}
$$

C_{in} being the total input impedance, in our case $C_{cap} + C_f$.

For the total system, we have:

$$
\begin{aligned}
I_{err}(s) &= (I_{in}(s) + I_0(s)) \frac{-R_{cap}\alpha - 1}{C_{in} R_{cap} s + R_{cap}\alpha + 2} \\
Q_{err}(s) &= I_{err}(s) \cdot \frac{1}{s} \\
V_{OTA_{in}}(s) &= (I_{ion}(s) H_{in}(s) + H_{I_0}(s)) \frac{1}{1 + \alpha H_{err}(s)}
\end{aligned}
$$

The offset ϵ_1 will be neglected, as for the worst case in both offset, resistance and integration time, the charge error is of $\sim 1\,\mathrm{fC}$, several order of magnitude smaller than the smallest pulse of interest.

Results are shown in figure 23. It can be seen that there is no impact from the insulation resistance on performance.

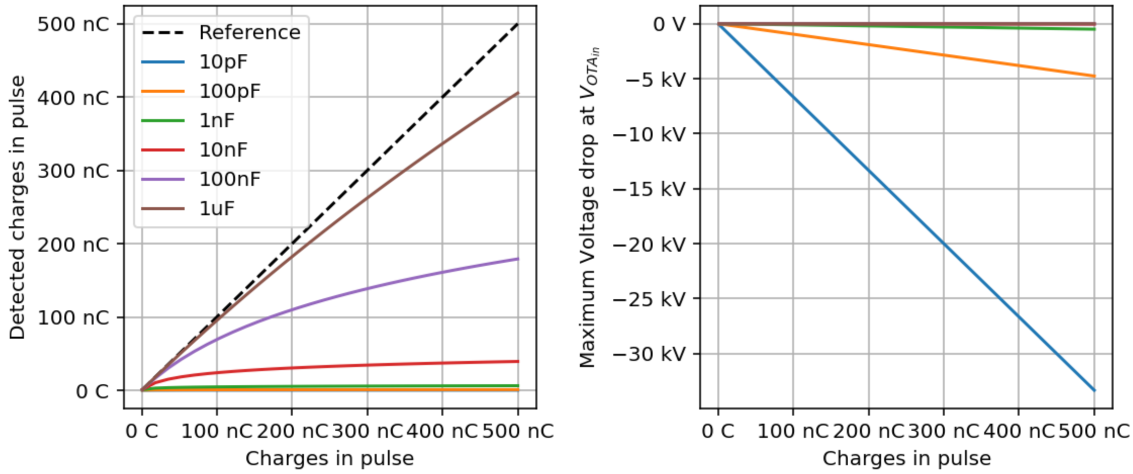

Figure 23: Pulsed behaviour of capAccurate for kronecker delta type discharge

3.3 Simple Twin Accurate

Using two Accurate may seem like a solution to the pulsed inaccuracies, as increasing the current that our system can deliver can extend the range of the linear range case to cover bigger pulses, and absorb more quickly charges when the system is in saturation.

However, as soon as the system gets in the saturation regime, no improvements whatsoever can be obtained. This stems from the fact that the $\alpha \sim C_{cp}$ dictates not only the current delivered to the input in case of saturation, but also the amount of excess charges. As the impact of having multiple Accurate in parallel is to augment C_{cp} by a factor, both the detected and excess charges are scaled up by the same amount. This is not to say that there is no possible beneficial effect in having two Accurates in parallel, as the increased current may be interesting for more complex input topologies, as well as the reduced time to absorb charges and increased linear range.

3.4 Capacitor Ladder

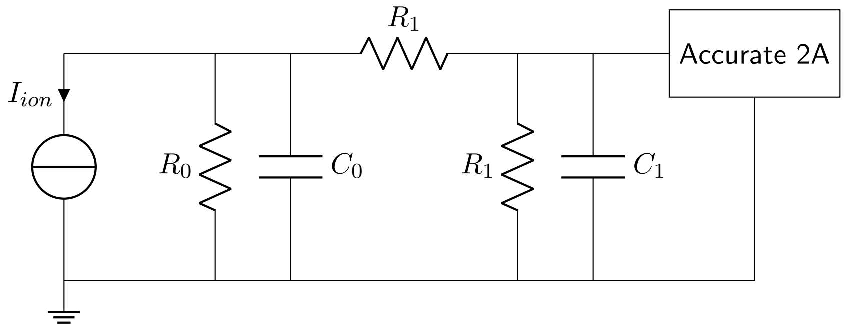

Figure 24: Block diagram of Accurate with a capacitor ladder

The idea of the capacitor ladder stems from the encouraging results for pulsed regime given by adding a $50\,\mathrm{M\Omega}$ resistor in a previous test, as described in [19]. This makes sense, as adding a resistor implements a low pass filter at the input of Accurate, thus reducing the maximum instantaneous input current during a pulse.

Using a resistor has few advantages:

1. Resistors do not leak to ground.
2. They allow a voltage drop between the ionization chamber and the OTA input, which can help minimize deviation from V_{cm}.
3. More control over the transfer function: By using a resistor, it may be possible to increase pulsed accuracy while keeping the input capacitance constant.

A few disadvantages can also be found:

1. Depending on I_{in} and the value of the resistor, a significant voltage drop can happen between the input of the OTA and the input of the device. In extreme cases, that voltage drop may interfere with the ionization chamber operation and/or leakage.
2. Due to external capacitance such as a cable, $V_{OTA_{in}}$ may reach V_{cm} while all charges contained in the pulse have not been collected, leading to a longer time to fully absorb it.
3. Johnson–Nyquist and $1/f$ noise can be an issue for large resistance values.

As the effect of the voltage guard miss-match with V_{cm} has been explored in section 3.2.1, it will be considered zero here.

3.4.1 Non-saturating Regime

Because there is now one more voltage node and thus one more line on the matrix to be inverted, it is significantly harder to solve the system analytically, even with computer-assisted method such as sympy. For this reason, a numerical method will be used. Programs such as SPICE could have been used, but since their time-step is usually constant, simulations for low currents can take a tremendous amount of time to complete even a single cycle, while modern methods allow for a variable step size based on error estimation, allowing the current estimation to simulate much faster than implemented methods methods. Finally, SPICE programs usually do not allow for proper digital control of the system, which make the charge pump behaviour impossible to cleanly simulate (i.e: once it starts activating, it must stay active for T_{co}).

Let us start by finding the equation systems defining the system. Let V_0 and V_1 be the voltage at C_0 and C_1, respectively.

Current Integration Using Kirchoff's law, the following is obtained:

$$0 = \frac{V_0}{R_0} + V_0' C_0 + \frac{V_0 - V_1}{R_t} + I_{in} \tag{33}$$

$$0 = \frac{V_1}{R_1} + V_1' C_1 + \frac{V_1 - V_0}{R_t} + g_m (V_1 - V_0) \tag{34}$$

The derivative form is then trivially obtained:

$$\begin{pmatrix} V_0' \\ V_1' \end{pmatrix} = \begin{pmatrix} \frac{-1}{R_0 C_0} - \frac{1}{R_t C_0} & \frac{1}{R_t C_0} \\ \frac{1}{R_t C_1} & -\frac{1}{R_1 C_1} - \frac{1}{R_t C_1} - \frac{g_m}{C_1} \end{pmatrix} \begin{pmatrix} V_0 \\ V_1 \end{pmatrix} + \begin{pmatrix} -\frac{I_{in}}{C_0} \\ V_{cm} \frac{g_m}{C_1} \end{pmatrix} \tag{35}$$

Charge Pump Connection Using the same approach, we obtain:

$$\begin{pmatrix} V_0' \\ V_1' \\ i_{cp}' \end{pmatrix} = A \begin{pmatrix} V_0 \\ V_1 \\ i_{cp} \end{pmatrix} + B \tag{36}$$

$$A = \begin{pmatrix} \frac{-1}{R_0 C_0} - \frac{1}{R_t C_0} & \frac{1}{R_t C_0} & 0 \\ \frac{1}{R_t C_1} & -\frac{1}{R_1 C_1} - \frac{1}{R_t C_1} - \frac{g_m}{C_1} & \frac{1}{C_1} \\ -\frac{1}{R_t C_1 R_{cp}} & \frac{1}{R_1 C_1 R_{cp}} + \frac{1}{R_t C_1 R_{cp}} + \frac{g_m}{C_1 R_{cp}} & -\frac{1}{C_1 R_{cp}} - \frac{1}{C_{cp} R_{cp}} \end{pmatrix} \tag{37}$$

$$B = \begin{pmatrix} -\frac{I_{in}}{C_0} \\ V_{cm} \frac{g_m}{C_1} \\ -V_{cm} \frac{g_m}{C_1 R_{cp}} \end{pmatrix} \tag{38}$$

Initial Conditions Because the numerical simulation iterates on time, one must provide initial conditions. In the present case, the steady state value cannot be found from the above equations alone, as the devices goes through multiple stages w.r.t the time. It can however be expected that the true steady state should be relatively close to the steady state of the DC circuit. In order to avoid errors in the charge counting, the simulation will be run for 100 cycles before making any measurement and any suspicious results are checked and rerun if necessary. For high currents and resistance values, the tests are typically run for a much longer time (800 cycles).

It follows:

$$V_{0_{initial}} = V_{cm} - I_{in} R_0 \frac{R_t (R_1 g_m + 1) + R_1}{(R_0 + R_t)(R_1 g_m + 1) + R_1} \tag{39}$$

$$V_{1_{initial}} = V_{cm} - I_{in} R_0 \frac{R_1}{(R_0 + R_t)(R_1 g_m + 1) + R_1} \tag{40}$$

Simulation Parameters The simulation was made using the python library scipy. The charge pump connection step was simulated using the explicit Runge-Kutta method of order 8, as it is the recommended method for high accuracy. Its usage does not impact significantly the performance of the simulation, as its duration is constant at T_{co}.

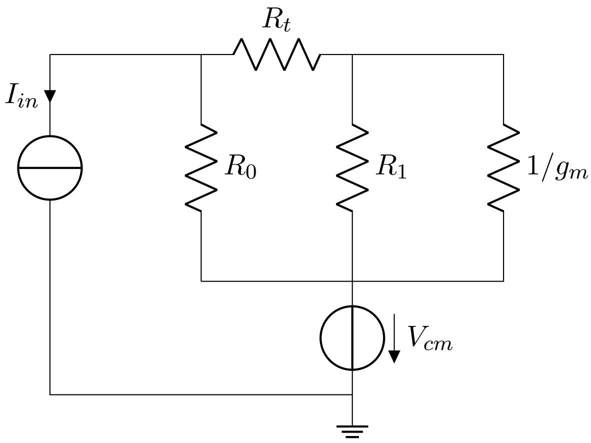

Figure 25: Diagram of DC state of Accurate with a capacitor ladder

The current integration step was simulated using the Radau method, as the problem exhibits stiffness issues. A maximum step size of $T_{ci_{ideal}}/1000$ was however set, as the increase in step size (and thus speed of computation) impacted the time at which the threshold crossing was detected.

Simulation Results As the aim is to limit the leakage current, the system was simulated using a single capacitor $C_0 = 10\,\mathrm{nF}$ with the maximum insulation resistance of $100\,\mathrm{G\Omega}$. C_1 was set to a low value that did not affect the stability of the simulation, $10\,\mathrm{pF}$.

Figure 26 show the simulation results. It can be seen that the addition of the resistor does not significantly impacts the accuracy of the device, even if there is a voltage difference between V_0 and V_{cm} due to the current passing through R_t (and thus, leakage through R_0). That can be explained by the fact that the ratio R_t/R_0 is very low for all datasets. The limit of the charge pumps can also be seen here, at $\sim 70\,\mathrm{\mu A}$.

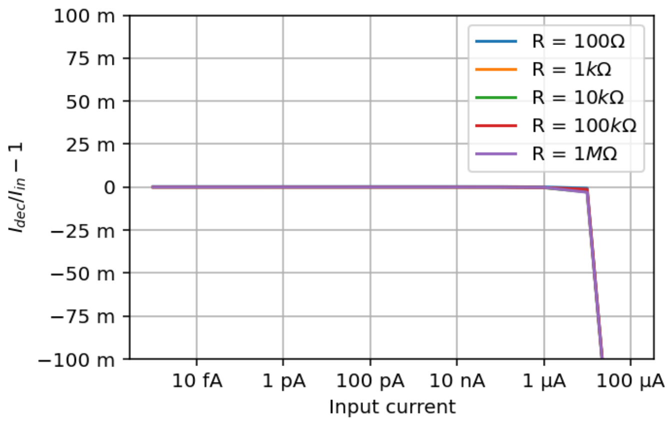

Figure 26: Relative error of Accurate with a capacitor ladder

More things can be done with this model. For example, the presence of double triggering of the charge pumps can be seen in simulation, which is something that is not possible to do with the current analytical model. It is also possible to input any arbitrary input current, so long as it would not put the real device in saturation. This could be interesting because it would allow to simulate accuracy for currents with a nonzero derivative w.r.t the time. Using the same method, it would also be possible to see the delay between a change at the input and the corresponding readout.

3.4.2 Saturating Regime

The transfer functions for Accurate with a capacitor ladder can be obtained with the same approach than for bareAccurate. It is however important to account for the leakage in addition to the excess charges delivered by the charge pump in order to find the losses in the charge detection:

$$Q_{err_{tot}} = \int_0^{t_{end}} I_{err}(t)dt + \int_0^{t_{end}} \frac{V_0(t)}{R_0}dt + \int_0^{t_{end}} \frac{V_1(t)}{R_1}dt \qquad (41)$$

This can be done in the Laplace domain, but one must be careful about taking into account the contributions of I_{err}, I_{in} and I_0.

From this, figure 27 is obtained. It can be seen that a resistor can indeed improve the collection of charges during a pulse, and that the value when benefits starts showing is around $10\,\mathrm{k\Omega}$.

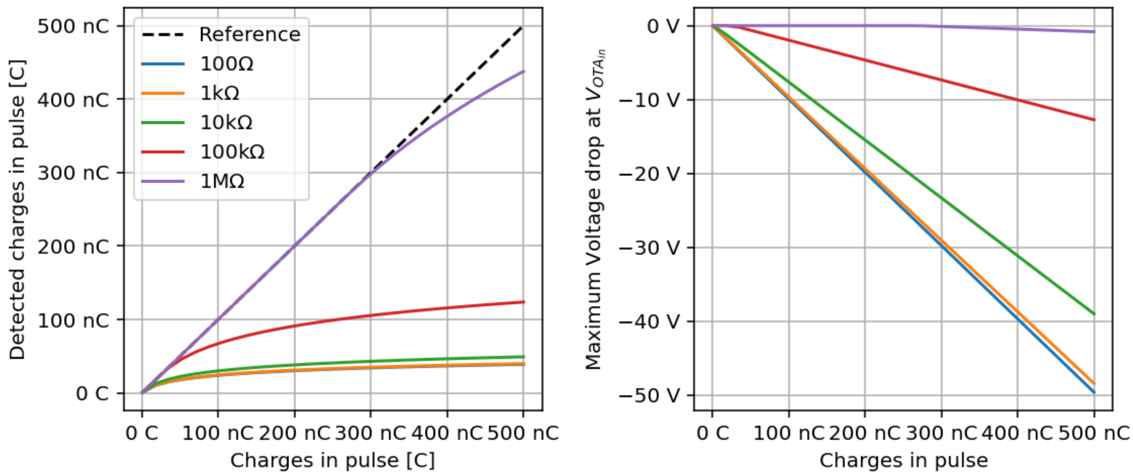

Figure 27: Pulsed behaviour of Accurate with Capacitor Ladder for Kronecker's delta type discharge

3.5 Twin Accurate

Early in the thesis, it was thought that the increased capacitance may affect the accuracy of the results. For this reason, twin Accurate, depicted in figure 28 was designed. The idea was to use a large capacitor at the input of the second Accurate and to "hide" it from the input using the resistor R_t. In static regime, the first Accurate (A1) would be active, with a low leakage current from the input to the second Accurate. In pulsed regime, A1 would saturate quickly and charge pumps for it would be disabled. Because the voltage drop across R_t would no longer be small, a current would flow through it, allowing the second Accurate to kick in with a large input capacitance, and thus lower error in the readout than A1.

With the knowledge acquired during the rest of the thesis, it was shown that it was not the capacitance which affected the accuracy of the device, but rather the insulation resistance of the capacitor and the voltage offset between V_{guard} and $V_{OTA_{in}}$, making this approach no better than capAccurate.

As this device was produced, experimental results for it will be presented, but the theoretical model will not be done, as the time it would take can be better spent elsewhere. Such a method could however be used in the future, for example with ladder Accurate, so that it is quick to respond in static regime, but has a large time constant in pulsed regime.

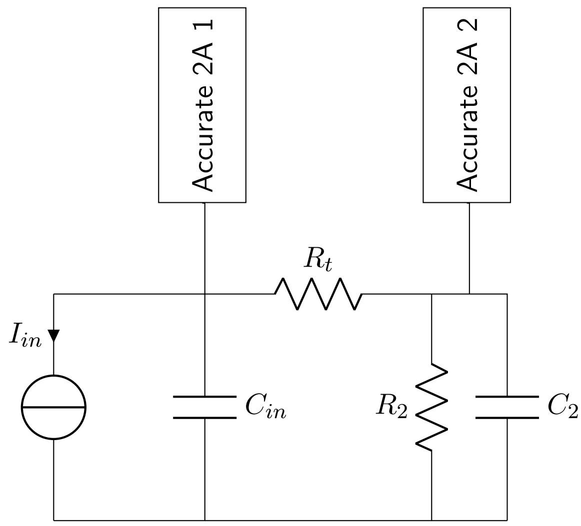

Figure 28: Block diagram of twin Accurate

4 Design of the New Testboards

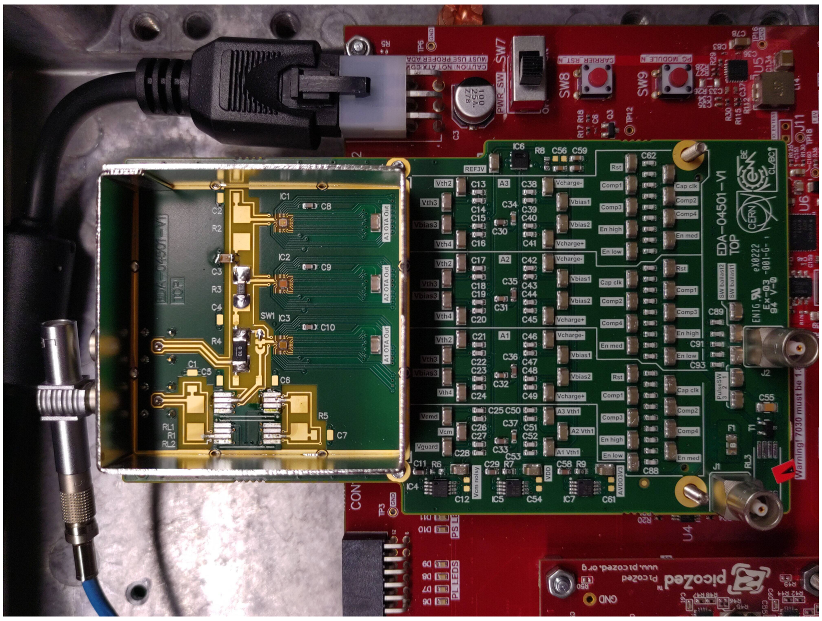

Figure 29: Picture of the development board in the twin Accurate configuration, mounted on the carrier board

In order to see whether the theoretic improvements of cap and twin over bareAccurate, two testboards were designed and produced with the collaboration with CERN's TE-MPE-EM section, and then tested in real scenarios (see section 6).

4.1 Input Circuitry

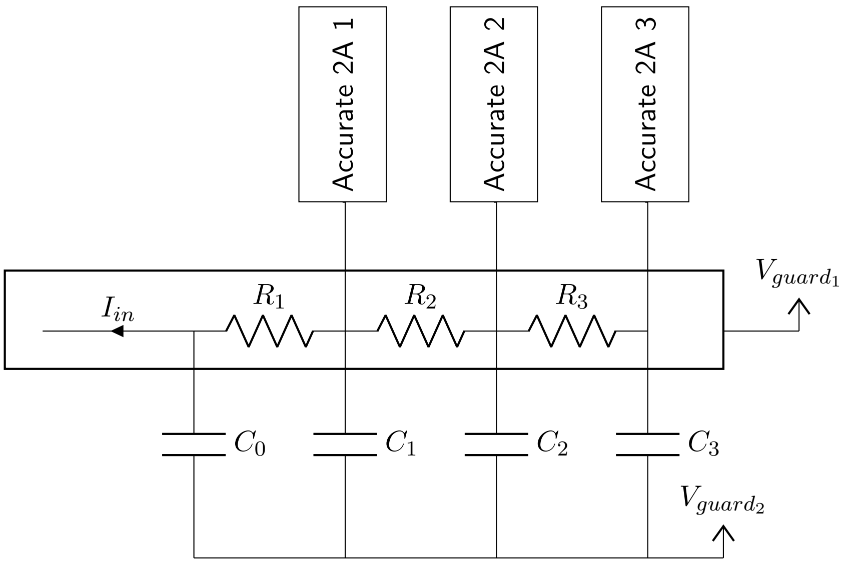

Figure 30: Block diagram of the input circuitry of the prototype testboard. Parasitic values ignored.

As the design, production and bonding time for a PCB are quite long and expensive, it was decided to use three ASICs instead of two. This leaves the possibility of testing more complex topologies in the future (for example, an Accurate could be used to compensate positive input currents). For the rest of this document, C_0, R_3, and C_3 will not be mounted and R_1 will be short-circuited.

Both V_{guard} should be set as close as possible to V_{cm}, so that leakage are minimized. Two different voltage were used for connecting the capacitors and the actual guard to increase flexibility and decouple their current requirement, as V_{guard_1} should not require any specific current requirement, whereas some peak currents can go through the capacitor during pulses and at power on.

In order to increase the insulation resistance between the input and the rest of the system, no conformal coating was used on the input.

4.1.1 Component Values Chosen

CapAccurate As the aim of the the thesis is to evaluate the possible improvements to the pulsed regime of Accurate, it was chosen to use the capacitor with the biggest value of $470\,\mathrm{nF}$. If the leakage due to the reduced insulation resistance and voltage offset causes issues to linear operation of the device, it may be quantified and thus requirements about the capacitor specification can be made. This is opposed to the situation where a low value capacitance is used and is not enough to produce significant results, thus not increasing knowledge about the potential of this approach.

C_1	R_2	C_2
$470\,\mathrm{nF}$	∞	N/A

TwinAccurate For the same reason, the selected capacitance for twin Accurate is also $470\,\mathrm{nF}$. Preliminary model in LT Spice suggested that a resistor of $47\,\mathrm{k\Omega}$ would be well suited for pulsed regime. Because of issues mentioned in section 3.4.1, evaluation of the impact in static regime for current lower than hundreds of nano ampere was not performed.

C_1	R_2	C_2
$0\,\mathrm{nF}$	$47\,\mathrm{k\Omega}$	$470\,\mathrm{nF}$

4.2 Additional Devices

Ti's DACs 7578 were used to provide the different voltages required by the ASICs. Because 9 different voltages are required per device in addition to V_{cm} and V_{cmd} that can be shared, 4 different 8-channel DACs were used. They are connected to the Zynq system via an i2c interface.

Moreover, since the DACs would share the i2c bus with the SHT21, a humidity and temperature sensor on the complete CROME integration, it was decided to also use this sensor on the board.

4.3 Interface with the Zynq Platform

Because of the relatively high pin count of the three ASICs (10 per device), the FMC LPC connector was used to connect the carrier board with the front-end. As the ordering of the pins are a standard, it would be straighforward to use the new front-end with a different carrier board/SoC.

5 CROME Integration

In addition to the development of the front-end topology, work was done to integrate Accurate 2A in the current production framework, CROME.

This was done so that Accurate gets closer to being production-ready, but also because previously developed tools can then be used for debugging, such as real-time data monitoring, automatic saving of the data to the cloud, easy export of the data to .csv files and real-time variable configuration. The operation of a CROME system was described in section 1.4.

5.1 Change of Carrier Board

In order to ease the development and reduce the amount of work needed for the prototypes, a PicoZed™ FMC Carrier Card V2 was used instead of the custom carrier board used for the production device.

Some work was required to make to transition the code to the new board, namely:

- Remove connection to non-existent devices: certain components, such as a temperature sensor, a CPLD and different indicators that do not exist on the new board had had their implementation removed. Proper care was needed to avoid faults further down the line by setting proper static values to replace the dynamic ones.
- Clock generation: the CROME system uses an external, high-quality clock for the PL. While a potential substitute is present on the board, its complex proprietary interface made the usage of an internal clock of the Zynq more efficient concerning the amount of work required. This does not impact significantly the operation of the device, as the main reason for using an external clock is keeping the time in sync over a long time, whereas this prototype will only make measurements spanning a few hours.

5.2 I2C Devices

The DACs used for setting the different voltages required by Accurate communicate using I2C. Thankfully an I2C master was already implemented in CROME, to communicate with the SHT21 temperature and humidity sensor.

The first thing that had to be done was to decouple the master from the SHT21 controller, as everything was done in the "Temperature and Humidity" module. Then a controller for the DACs was written, as well as an arbiter. The general architecture is depicted in figure 31.

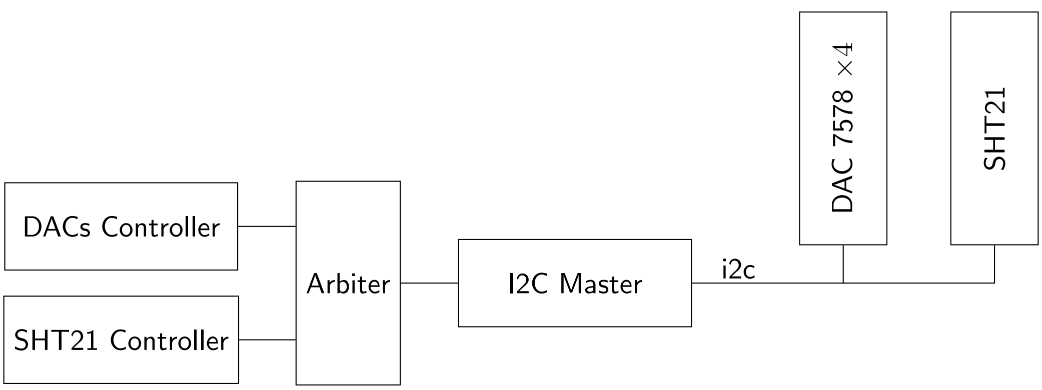

Figure 31: i2c architecture for the integration of Accurate

5.2.1 Master

Once that was done, the master was rewritten so that:

- It can send commands of arbitrary length (as opposed to only 8 bit commands).
- It has better compliance with i2c:
  - No half cycle wasted when waiting for acknowledgement of slave.
  - No full cycle lost when stopping communication.
  - Correct Stop signal.

One improvement that could be done on the current version is to regularise transactions. For example, the address and the command(s) are currently handled differently in the master final state machine, even though they are handled in the same way.

5.2.2 SHT21 Controller

While the interface of the SHT21 controller was modified to reflect the changes in the master module, the core functionality has not been modified, with the exception of the error handling. Previously, when a transaction failed (because of a hardware failure of the sensor, for example), it was retried immediately without any sort of time out, effectively spamming the bus. Moreover the readout was kept constant and no error was raised. This has been modified so that, if an arbitrary number of consecutive communication failures happen, the attempts stop and an error is reported to the fault monitor.

5.2.3 DACs Controller

The DACs controller works by keeping track of all the voltages it has programmed in an array and comparing it to the values given by the PS. When a missmatch happens between the forwarded values and the internal array, the first one is picked and saved in a special register, as well as its index[6]. The controller will then initiate a communication with the master and update the internal array if the transaction was successful.

The DAC controller behaves similarly than the SHT21 controller in terms of how communication and errors are handled.

5.2.4 Arbiter

Now that the DACs controller and the SHT21 wants to talk to the i2c master, the need for arbitration arises. While the specification of the i2c bus allow for multiple master connected physically on the bus, the current i2c master does not support it. Adding that support would be a waste of resources, as the connection to two different master would have to happen in hardware, since there is no tri-state buffers dedicated to connections inside of the PL. Moreover, as the two different controllers communicate relatively rarely on the bus, a simple arbiter can provide satisfactory results.

This simple arbiter works in a first-come first-served manner and will give more importance to the DACs if both controllers want to talk at the same time. It has been implemented in combinational logic only (except for remembering which controller is currently in transaction), so

[6]This is so that if a new value is written at the beginning of the array during the transaction, no confusion can happen

that no modifications for accommodating the arbiter is required in the existing design. It would be possible to add a register delay if proper care is taken with the signal starting the transaction ($start$).

5.3 Accurate 2

The actual integration of Accurate in CROME is straightforward, thanks to the modular approach already existing in CROME. Indeed, a module dedicated already exists solely on interfacing with the front-end and providing two signals, $VoltageChangeInterval$ and $VoltageChangeIntervalRdy$ after the control signal $windInterval$ is high. In order to make the new module fully modular with the current CROME implementation, the only trick is to provide the integrated charge over the last interval translated to an "CROME front-end equivalent voltage".

Since T_{co} is in the order of tens of nanoseconds, the default PL clock of $20\,\mathrm{MHz}$ is not fast enough. Thus, an additional clock has to be instantiated in the design and clock domain crossing must be implemented.

The general architecture of the front-end is show in figure 32.

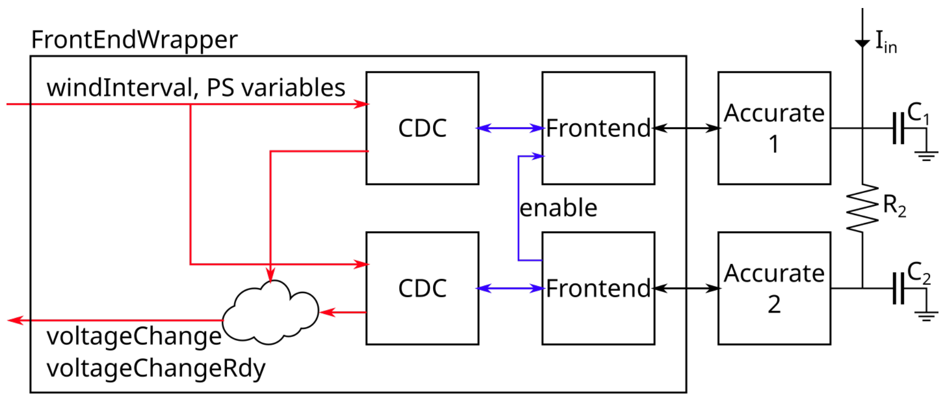

Figure 32: General Architecture of the front-end. The second channel can be disabled and R_2 removed for single ASIC operation. The different colours indicate the change in clock domains.

5.3.1 Accurate Frontend

The signal used in the Accurate to front-end interface are shown in table 1. In order to simplify explanations, all signals are supposed active high in this section, though it is not always the case in the real device.

Signal Name	Direction	Clock	Description
V_{comp_N}	in	$\varnothing$	Corresponding threshold reached.
V_{enable_N}	out	cap_clk	Corresponding charge pump activation.
cap_clk	out	N/A	Defines the timing of the charge pumps.

Table 1: Interface between Accurate and the CROME front-end. Directions are relative to CROME.

It is worth noting that V_{comp_N} is not clocked, thus a double flip flop will be used on the input. Also, due to Accurate's internal structure, V_{enable_N} must be asserted and de-asserted synchronously with cap_clk. The truth table for these signal is provided in table 2. Arbitrary values can be set for the duration of the low and high cap_clk times. The low duration represents T_{co} and the high, the minimum T_{ci} possible (this is done to allow the charge pumps to reach steady state before the next activation).

V_{enable_N}	cap_clk	C_{cp_N}
0	X	Both sides in high impedance
1	0	Both sides connected to V_{cm}
1	1	Connected to V_{cp} and $V_{OTA_{in}}$

Table 2: Effect of V_{enable_n} and cap_clk on the charge pump

The implementation of the front-end is shown in figure 33. It can be seen that each of the charge pumps' channel is similar to one another. First the comparator signal goes through a double flip flop to avoid metastability. Then it is sampled according to the start of each cap_clk cycle, and send back to the ASIC. Moreover, if a high signal was detected, the corresponding $V_{th_N sum}$ is notified.

What this block does, is that instead of simply counting the pulse, which would result in a lot of computation at the end of each t_{sample}, a register is incremented by a value settable by the user. As the output value of the Accurate block must be a CROME equivalent voltage sum, one must find the CROME equivalent code $V_{th_N conv}$ for the charge that the charge pump injects:

$$Q_N = C_{cp_N}(V_{cp} - V_{cm}) \quad (42)$$

$$V_{OTA_{out}CROME}N = Q_N / C_{f_{CROME}} \quad (43)$$

$$V_{th_N conv} = \frac{V_{OTA_{out}CROME}}{2V_{range}} 2^{24} \quad (44)$$

$$= \frac{C_{cp_N}}{C_{f_{CROME}}} \frac{V_{cp} - V_{cm}}{2V_{range}} 2^{24} \quad (45)$$

The factor 2 in front of V_{range} comes from the fact that a differential ADC is used, and the 2^{24} beacause the ADC has a resolution of 20 bits, left extended in the PL with 4 additional bits.

Finally, when $windInterval$ is asserted, the result from the three summation blocks are added together and provided at the output. Because this is done in a single cycle, the ready signal is simply a delayed version of $windInterval$.

$V_{th_1 comp}$ is a "free" comparator, in the sense that it does not have a corresponding charge pump. It can be used for various purposes, such as implementing a direct slope measurement method, or to detect positive/negative saturation of the device. In our case, this signal will be left unused, except for the ASIC taking care of the pulsed regime, where it will be used to detect a pulse event.

5.3.2 Clock Domain Crossing (CDC)

In most cases, a two flip-flop synchronizer has been used. Concerning $windInterval$, as a single cycle high pulse is required, edge detection is performed.

It is worth noting that, in the current state, $windInterval$ and the PS parameters are *not* synchronized. A more complex CDC is required for this to be possible. $voltageChangeRdy$ is the most complex signal to transmit, because it is a fast, single pulse signal going from a fast clock to a slower one. The method used here is a simple handshake, which ensures that the signal has been properly detected in the destination clock domain before de-asserting it.

Even if $voltageChange$ crosses a fast-to-slow clock boundary, no particular logic is required apart from a two flip flop synchronizer. This is because its associated valid signal, $voltageChangeRdy$, is slower[7] to cross the boundary and that this signal can only change at t_{sample} rate, making it very low frequency.

[7]at least one cycle of the slow clock

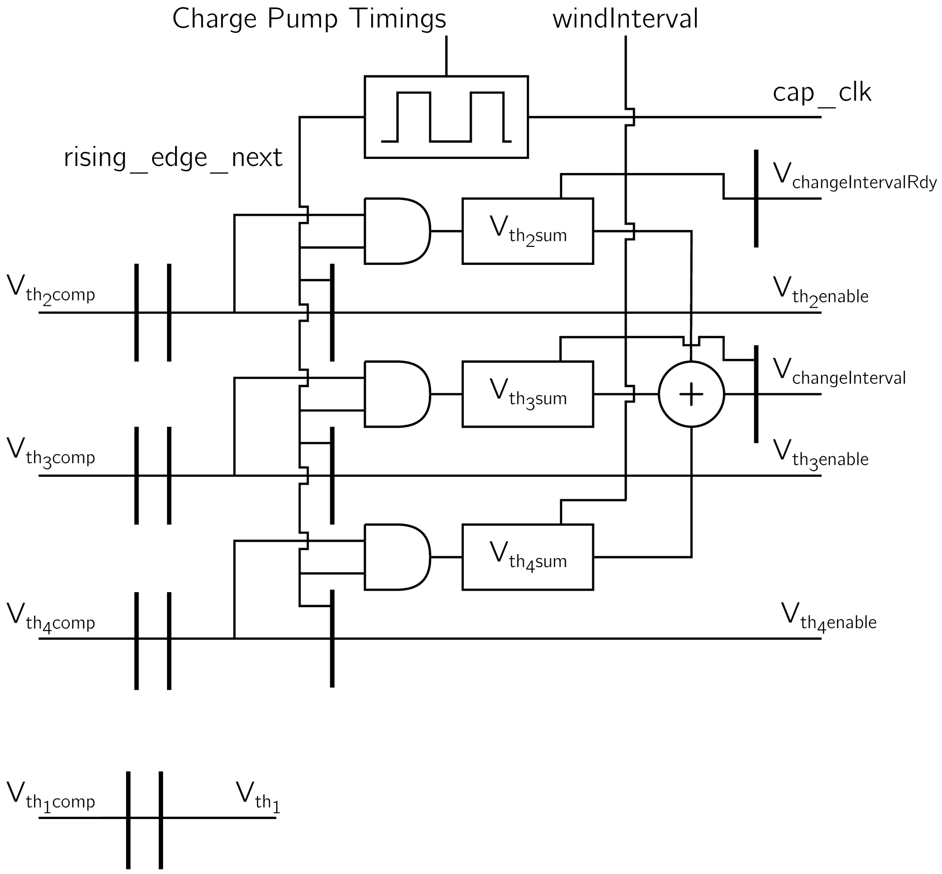

Figure 33: Implementation of the Accurate interface. Not depicted: PS variable representing the equivalent voltage for each pulse of $V_{th_N sum}$.

The implementation is depicted in figure 34.

5.3.3 Alternative to Regular Front-End

It has been mentionned in section 2.1.4 that, ideally, the activation of the charge pumps should all be equally spaced in time to avoid loss of resolution, mainly. Such an issue can be mitigated inside of the front-end by using a cooldown-type mechanism based on the last two activation. For example, if the last two activation were spaced by $10\,\mu s$, then the next activation would be forbidden in the next $5\,\mu s$. Moreover, as the most critical time is right after the activation, a maximum cooldown can be implemented, so that decent reactivity to fast change in current is insured. A good starting point for setting this maximum cool-down could be a multiple of the reaction time of the OTA, τ_{sys}.

Another potential benefit of this approach is that when using two Accurate ASICs on the input and an pulse happens at the input, we usually want to disable the chip in charge of the static current before its activation causes errors in the readout. Using a slow-start front-end would give more time to actually detect the pulse, while having no impact on the operation of the device in high static current scenarios.

Because the double-triggering effect of the charge pumps is not a fully understood phenomenon and that this change in implementation could affect the performance of the device, it was decided to keep using a front-end implementation analogous to previous works, so that the hardware implementation is compared, instead of a mix of software and hardware. Nevertheless, a "slow"

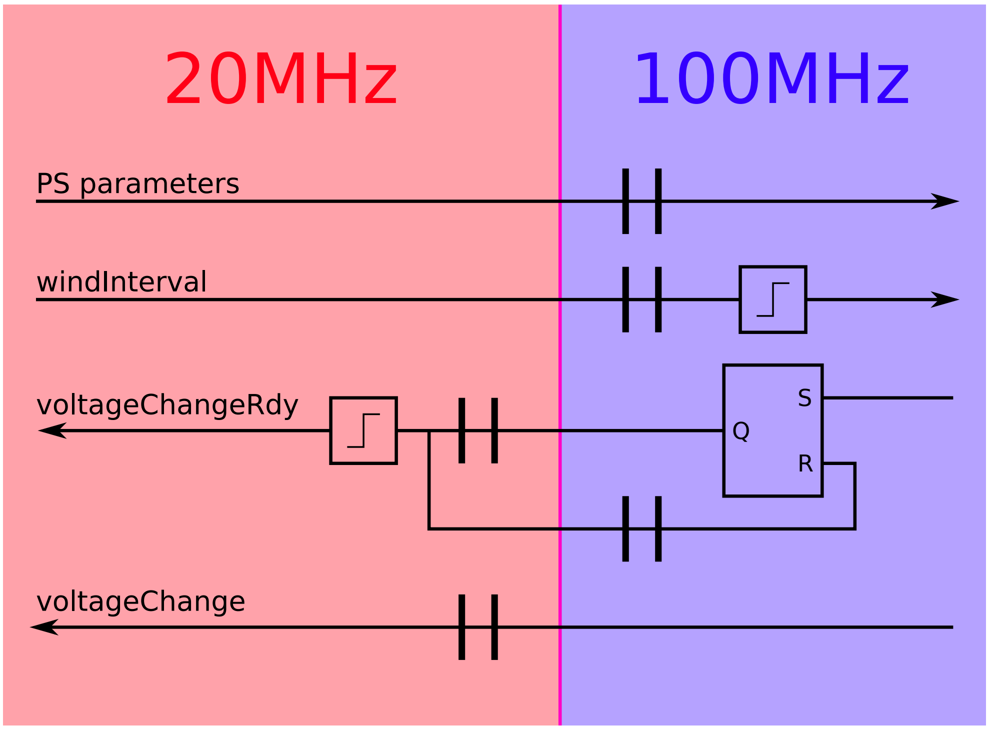

Figure 34: Implementation of Clock Domain Crossing for the Accurate front-end

front-end has been designed and could easily be tested on the new testboards.

5.4 PS to PL Modifications

Even though it is not planned to give any control of the front-end parameters to the end user, several values are settable in software for ease of debugging, namely:

- DAC voltages
- $V_{th_N conv}$
- Charge pump timings

The implementation of the parameters transmission between PS and PL piggybacks on the one already present in CROME. It was thus a matter of adding a few lines in the configuration files to make it work, and hard-coding the values inside of the CROME software. Thus, these parameters are not settable in real time, but instead one software compilation away, which is already a huge improvement over recompiling the HDL code ($\sim 2\,\mathrm{min}$ vs $\sim 1\,\mathrm{h}$).

6 Measurements

With the testboards completed, it was decided to test them at three different locations:

- Section's Lab: Our section is in possession of a Keithley 6430, capable of accuratly sourcing current from $0.5\,\mathrm{fA}$ to $105\,\mathrm{mA}$, which ideal for calibrating and testing the static regime of the device.
- Calibration Lab: The Calibration Lab at CERN is a dedicated facility for testing equipment under precise ($\pm 5\%$) radiation doses, ranging from $5\,\mathrm{\mu Sv\,h^{-1}}$ to $150\,\mathrm{mSv\,h^{-1}}$ [20]. The performance if the device in "real life" static regime was established there.
- IRA (CHUV): IRA graciously allowed us to use their eRT-6 particle accelerator. This device is capable of producing pulsed radiation in the same range than the CERN accelerators (a few $\mathrm{Gy\,min^{-1}}$ up to hundreds of $\mathrm{Gy\,s^{-1}}$)[21], which allowed us to determine the pulsed fields capabilities of the device.[8]

As much as possible, the tested prototypes (capAccurate and twinAccurate) were tested against both the original testboard of bareAccurate and the reference electrometer, the Keithley 6517B, so that the possible non-linearities from the ionization were removed from the equation. Moreover, all tests were done using Centronics' IG5 A20, with the same biasing voltage of $-1000\,\mathrm{V}$.

6.1 HSE-RP-IL (CERN)

6.1.1 Calibration

Due to the fabrication process of Accurate, the capacitance value of its charge pumps is not precisely guaranteed. Hence, they require calibration before the device can be used. The calibration philosophy used here was to try and determine as accurately as possible the capacitance of the charge pumps and *not* to compensate for any other type of error. In order to do this, an input current producing a low error in the measurement was used. Using figure 21 and figure 15, the value of $1\,\mathrm{nA}$ was chosen for its good trade-off between error due to the leakage and noise resistance.

Using the capacitance from the original bareAccurate testboard as a starting point, the linear error was assessed using a 1-hour long measurement and the known capacitance modified accordingly. As the first calibration was done using a shorter time ($10\,\mathrm{min}$) and without letting the temperature of the device reach steady state, a second calibration run was performed.

Future work could be done to find if the capacitance value of the charge pumps have a relationship w.r.t the ambient temperature.

6.1.2 Non-Saturating Accuracy

The non-saturating accuracy was performed by averaging the measurement over $1\,\mathrm{min}$ for currents above $100\,\mathrm{pA}$, and $10\,\mathrm{min}$ for all other values. The results are shown in figure 35. The voltage offset used for the simulation was determined using the first non-zero datapoint, like so:

$$I_{leak} = I_{in} - I_{dec} \approx 360\,\mathrm{fA} \tag{46}$$

$$\epsilon = I_{leak} R_{cap} \approx 780\,\mathrm{\mu V} \tag{47}$$

[8] It was initially planned to test the prototypes at CERN, using the PSAIF facility [22], but changes in the planning of CERN's operations prevented us from this.

	Initial Value $[fF]$	Relative Error$[\%]$	Corrected Value $[fF]$
C_{cp1}	454	-7.4	490.25
C_{cp2}	$1'060$	$+7.5$	985.98
C_{cp3}	$3'950$	$+4.8$	$3'768.82$

(a) First Round

	Initial Value $[fF]$	Relative Error$[\%]$	Corrected Value $[fF]$
C_{cp1}	490.25	$+0.6$	487.15
C_{cp2}	985.98	$+1.8$	968.76
C_{cp3}	$3'768.82$	$+1.1$	$3'727.75$

(b) Second Round

Table 3: Calibration of capAccurate

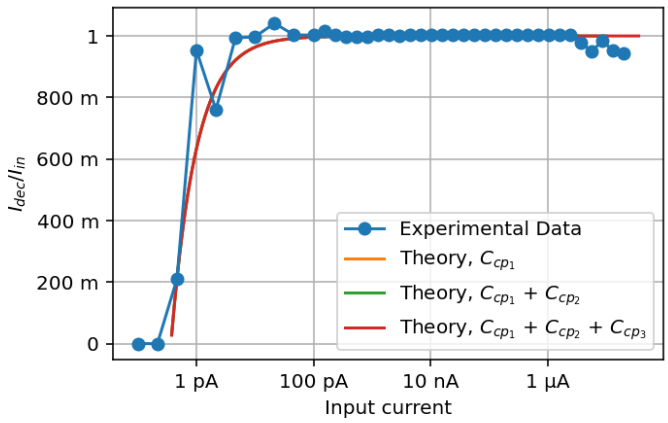

Figure 35: Experimental results for static regime of capAccurate. The theoretic values are obtained using the calibrated capacitances and takes into account the $2.9\,\mathrm{nF}$ capacitance of the cable. C_{cp_1} and $C_{cp_1} + C_{cp_2}$ data is hidden behind the last curve

Because noise is quite present at these values and that a single datapoint was used, the confidence in the value being precise is quite low.

The results are shown in figure 35. First, it is interesting to note the underestimation of the measured high currents, which is something seen in the theory, but with a much lower impact. This is likely to come by a combination of the discretization of the charge pumps' activation[9] and the current offset I_{in}/g_m[10]. Another unknown is the precise behaviour of the current source. If it reacts quickly to charge injection by raising its internal voltage, then it may affect the measurements, particularly in the high range.

Second, the leakage current/offset voltage is high, which prevents measurements at low currents. Because of this, it was tried to short circuit V_{cm} and V_{guard_2}, so that the DAC error is removed.

Results are shown in figure 36. The modification leads to a dramatic improvement of a factor $10\times$. Using the same method used previously, the leakage and offsets for the modified board are

[9]Due to the front-end structure in the PL, the charge pumps can only activate every $T_{co} + T_{ci_{min}} = 150\,\mathrm{ns}$. This was done to improve noise tolerance but may add noise at high currents, depending on the "super-period".

[10]With the theoretic $g_m = 3\,\mathrm{mS}$, an underestimation of the current of $\sim 0.3\%$ can be expected.

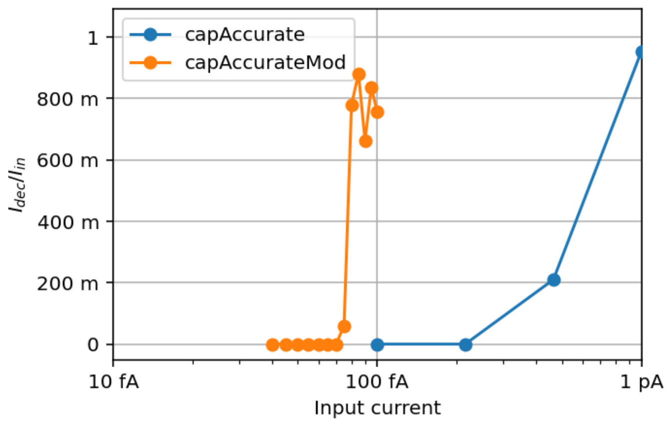

Figure 36: Effect of short-circuiting V_{cm} and V_{guard_2} for capAccurate

found:

$$I_{leak} \approx 70fA \quad (48)$$
$$\epsilon \approx 140\mu V \quad (49)$$

This offset should come primarily from the OTA's offset,

Given that bareAccurate's leakage has previously been evaluated in a controlled environment at $\sim 6\,\mathrm{fA}$, it can be speculated that using a capacitor with:

$$R_{cap_{new}} = \frac{I_{leak_{cap}}}{I_{leak_{bare}}} R_{cap} \approx 25\,\mathrm{G\Omega} \quad (50)$$
$$C_{cap_{new}} = \frac{1000 M\Omega\mu F}{R_{cap_{new}}} \approx 40\,\mathrm{nF} \quad (51)$$

Would result in a negligable increase in leakage current $(2\times)$, while providing a much better input capacitance in regard to pulsed radiation.

Moreover, the above-results show that the most important factor for the usage of Accurate with an input capacitor is the offset between V_{guard_2} and $V_{OTA_{in}}$ in steady state, as well as the insulation resistance of the capacitor used. It would be interesting to design the next version of the chip so as to minimize this offset, so as to either increase the low current range, or the maximum acceptable input capacitance.

Another interesting experiment which did not happen because of time constraints would be to check whether the leakage of the old and the new testboard for the same topology is equal, as the layout of the input circuitry is slightly different.

6.2 Calibration Laboratory

CERN's Calibration Laboratory features various different facilities for the calibration, characterization and evaluation of a wide range radiation-related devices. The facility of interest to us is the Gamma Beam Irradiator. This device provides different selectable radiation sources and a motorized table, which allow for a wide range of dose rates ($5\,\mu\mathrm{Sv\,h^{-1}}$ to $150\,\mu\mathrm{Sv\,h^{-1}}$) by changing the radiation source or its distance to the chamber. It can be noted that the high range of dose rates is limited by the physical dimension of our ionization chamber: as an homogeneous field is required for proper evaluation, it is not possible to get too close to the source.

The precise setup used is shown figure 37, and pictures of the actual setup can be found in figure 38.

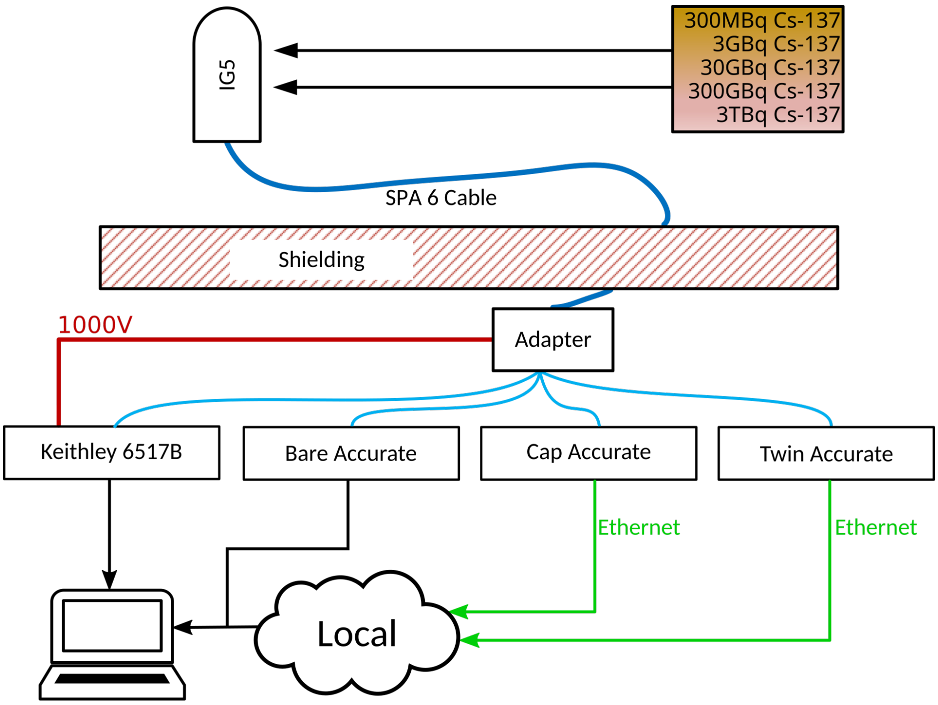

Figure 37: Setup used at CERN's Calibration Laboratory

One can note the motorized table, as well as the Gamma Beam Irradiator (brown device), which raises and lowers the specified radiation source for its body to its head (38a). BareAccurate with its required voltage source and recording is present on the left of (38b), while the reference electrometer, the adapter box, the cap/twinAccurate testbox (aluminium) and its recording computer are on the right.

6.2.1 Static Accuracy

Taking each datapoint as an average over one minute, figure 39 is obtained. Instead the values of a previous measurement made at the calibration laboratory were used, using the exact same setup (device, cable, ionization chamber, ...).

Good linearity can be seen for bare and capAccurate, even though there is a average linear difference between the two of 7.4%. As capAccurate was properly calibrated two days before the experiment, the proper calibration of bareAccurate can be put into question. It may be possible that exposure to elements (humidity, mainly) over a period of $\sim$ one year affected its intrinsic parameters, such as the charge pumps' capacitance.

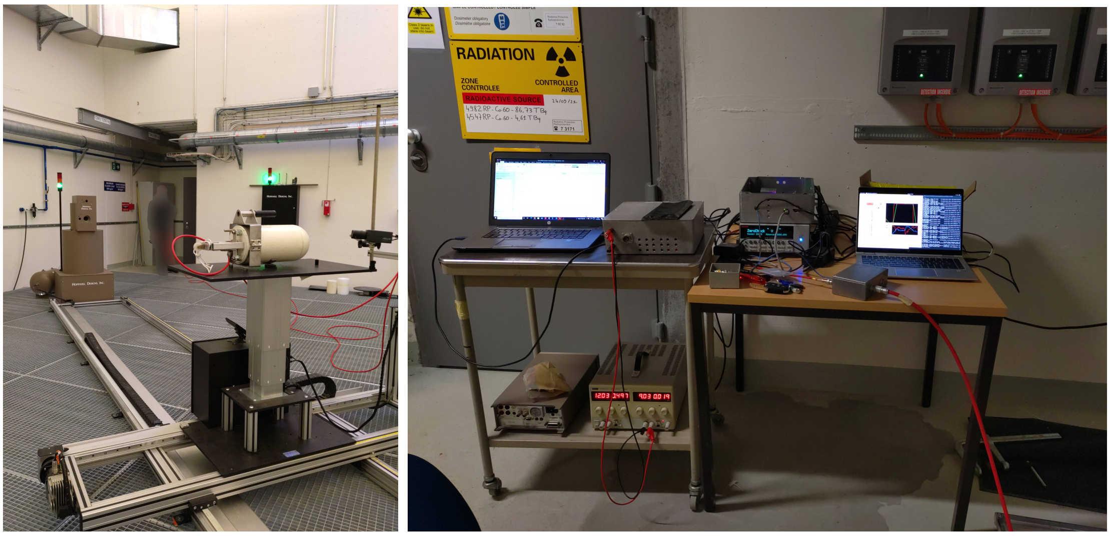

(a) Ionization chamber and Gamma Beam Irradiator

(b) Test devices and other necessary equipment

Figure 38: Physical setup used at the Calibration Laboratory

As the Keithley measurement were not made during the same test campaign, it cannot be determined with 100% certainty if the drop in the last point comes from a setup error, or from an issue in the design. Given that this non-linearity is well within the linear range of Accurate ($\sim 200\,\mathrm{nA}$) and that all tested devices exhibited this behaviour, the most likely explanation is that the ionization chamber was not properly centered on the motorized table (notice how the semi-spherical end sticks out on the right in figure 38a), thus causing a non homogeneous field when it was close to the source ($1\,\mathrm{m}$ in this instance). The linear difference between the Keithley and other devices can be explained by the fact that due to the radiation sources not being constant through time, small repeatably errors may happen.

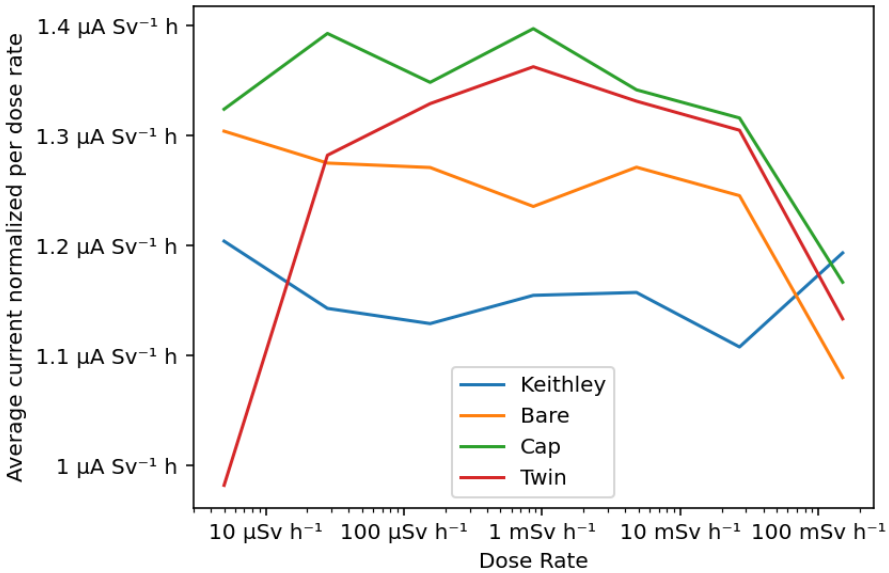

Figure 39: Average current normalized per dose rate from the Calibration Laboratory

6.3 IRA (CHUV)

Pulsed fields characterization of the new front-end was done at the Institute of Radiation Physics (IRA), who agreed to let us use their Oriatron eRT6 accelerator.

The test campaign at IRA had two main goals:

- Check the performance improvement of capAccurate over bareAccurate in pulsed regime.
- Improve understanding of the ionization chamber's model in pulsed regime, as the input current shape can have a sizable impact on the performance of Accurate.

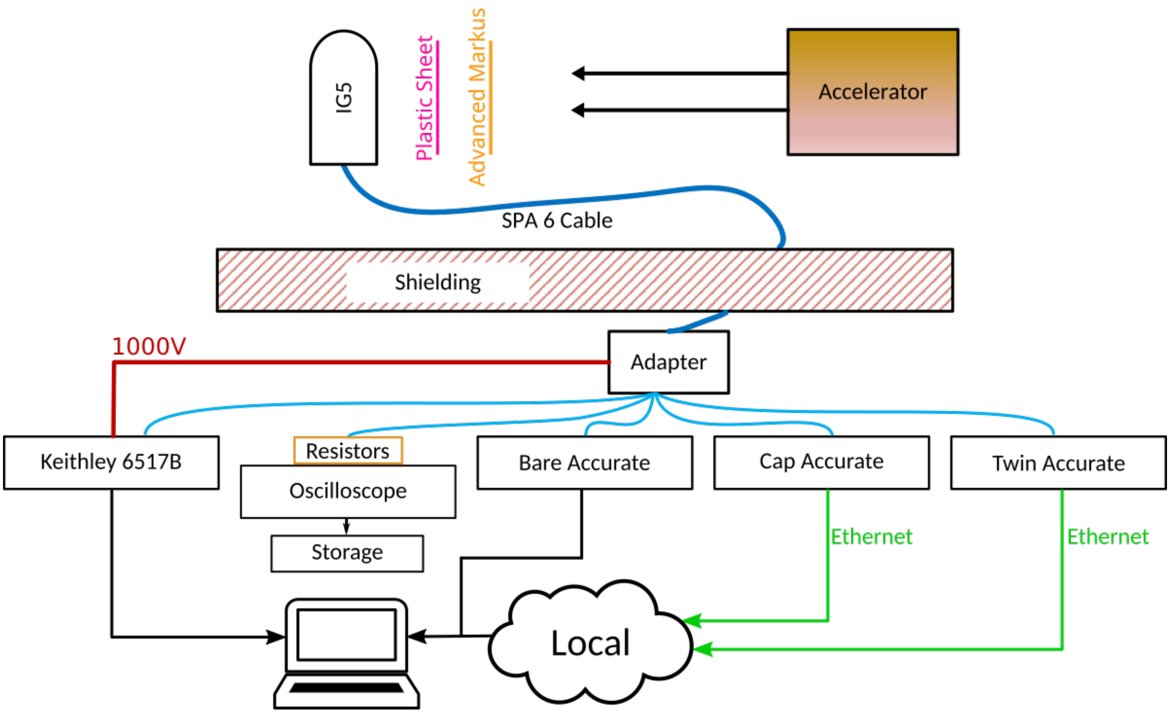

Figure 40: Setup used for the test campaign at IRA

A similar setup than the one used at the Calibration Laboratory was used, with the addition of an oscilloscope, as shown in figure 40. Moreover, one can note the presence a plastic sheet, used to convert the electrons to gamma rays, as well as IRA's monitoring system, connected to an Advanced Markus chamber. While it will allow us to see the intensity of the pulse, it is worth noting that the dose reported by IRA's system is not the same as the one the ionization chamber will be subjected to, as the plastic sheet and the Markus chamber will interact with the beam. These interactions should however be linear, so comparison between the dose detection capabilities of both systems should be possible.

Pictures of the physical setup can be found in figure 41.

One can note the red display in the left picture, indicating the distance from the movable table to the accelerator. The ionization chamber was centered and leveled using laser indicators. On the right picture, one can find the reference electrometer as well as the adapter box and test devices. The computer is running a CROME real-time monitoring software, reporting the current measurement (above), as well as the temperature and humidity reported by the SHT21 (below, in red and blue, respectively).

The accelerator metaparamters, as well as the oscilloscope setup will be described in more detail in the following sections.

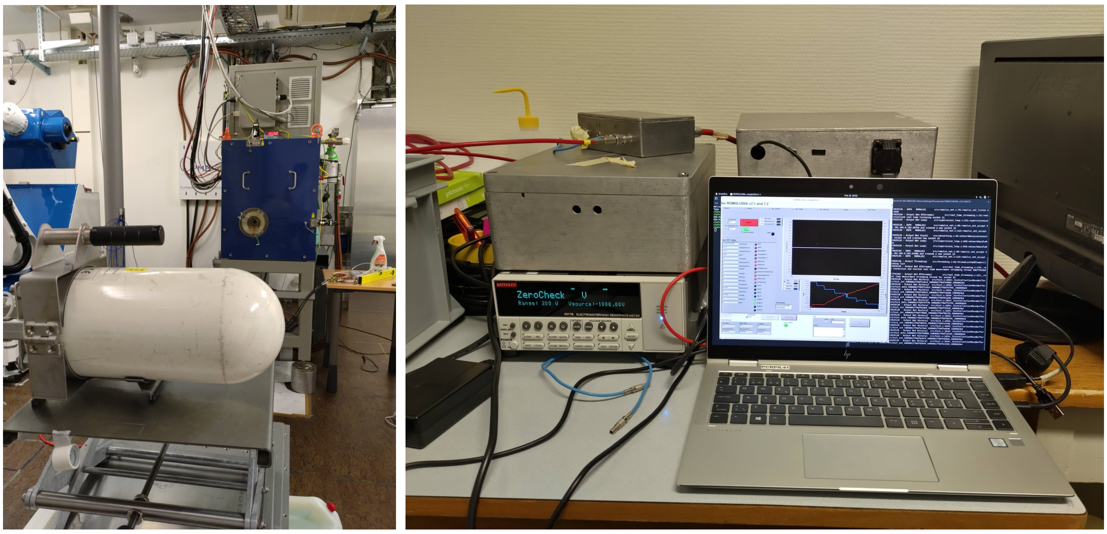

(a) Ionization Chamber and Accelerator **(b)** Test Devices

Figure 41: Pictures of the physical setup at IRA

6.3.1 The Oriatron eRT6 Accelerator

The Oriatron eRT6 is an experimental high dose-per-pulse linear accelerator (linac) which was designed to deliver an electron beam with variable dose-rates, ranging from a few $\mathrm{Gy\,min^{-1}}$ up to hundreds of $\mathrm{Gy\,s^{-1}}$. It was built to study the radiobiological effects of high dose-per-pulse/dose-rate electron beam irradiation, in the context of preclinical and cognitive studies. [21].

This accelerator uses a thermionic emission gun electron beam source, where electrons are extracted from the surface of a cathode brought to a high voltage ($10\,\mathrm{kV}$). The extraction of electrons is controlled by the grid voltage, which is located close to the surface of the cathode. The higher the grid voltage, the more electrons are extracted, and the more intense is the beam output.

Others parameters determined the generated radiation dose, such as the pulse width used for the grid excitation, and the pulse repetition frequency.

The ideal pulse train resulting pulse train is shown in figure 42.

6.3.2 Metaparameters Selection

While this accelerator has been characterized for its operating range, the range and resolution of dose-per-pulse needed for the performance evaluation of Accurate was not. Thus, the first step of the experimentation was defining the correct set of parameters, presented in table 4. The charge per pulse was found by taking the integral charge detected over the whole run and dividing it by N.

It was chosen to use a pulse train, as opposed to single pulse operation, because IRA's current monitoring system needs a few pulses to be reliable. Moreover, simulations and previous experiments show that Accurate is capable of reaching steady state in less that $10\,\mathrm{ms}$ with Kronecker's delta discharges of this amplitude, so a repetition period of $100\,\mathrm{ms}$ is not an issue in this regard.

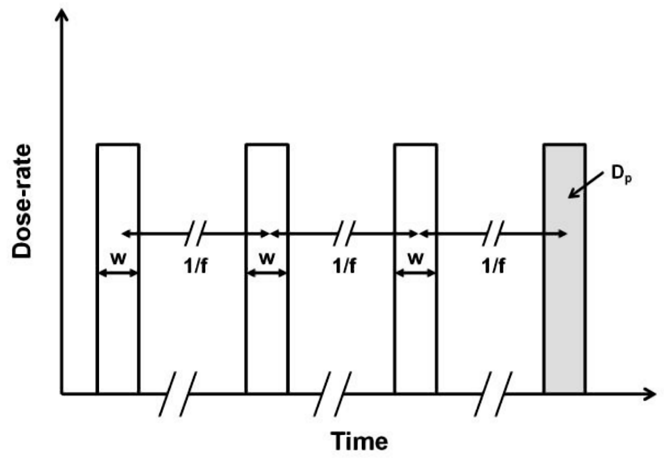

Figure 42: Ideal Pulse Train, with f the repetition frequency, w the pulse width. The dose-per-pulse D_p can be found by computing the area-under-the-curve for a particular pulse.[21]

Keithley CPP $[nC]$	GV $[V]$	$w[\mu s]$	d $[mm]$	f $[Hz]$	N
17	100	1.0	1900	10	100
91	120	1.0	1900	10	100
117	130	1.0	1900	10	100
140	140	1.0	1900	10	100
168	160	1.0	1900	10	100
183	180	1.0	1900	10	100
197	200	1.0	1900	10	100
200	250	1.0	1900	10	100
220	300	1.5	1900	10	100
226	300	2.0	1900	10	100
234	300	4.0	1900	10	100
270	300	4.0	1220	10	100

Table 4: Chosen metaparameters for the IRA test campain, with CPP the charge-per-pulse, GV the Grid Voltage, w the pulse width, d the distance from the accelerator to ionization chamber, f the repetition frequency, N the number of pulses.

6.3.3 Pulsed Accuracy

First, let us see the raw data reported by capAccurate, as presented in figure 43. It can first be noted that each individual pulse cannot be seen. This is because the repetition rate of the accelerator and the external sample rate of Accurate are equal. Second, the results are very reproducible, as noise on the results is very low. Finally, the data for the lowest charge per pulse (orange curve) does not follow the same pattern as the other ones. A proposition for this behaviour will be presented later in this section, after more data has been presented.

The obtained results for pulsed accuracy w.r.t the reference electrometer are shown in figure 44[11]. To improve the discussion, previous results made at PSAIF for bareAccurate are also shown.

The results do not follow the simulations, nor previous experiments. It is expected that the higher the charge-per-pulse, the less the test device is able to accurately report the charge, leading to a "saturation" phenomenon, as show by the "bare at PSAIF" curve.

Moreover, due to the same architecture, it should not be possible for a properly calibrated

[11]The normalized version can be found in the appendix, figure 56

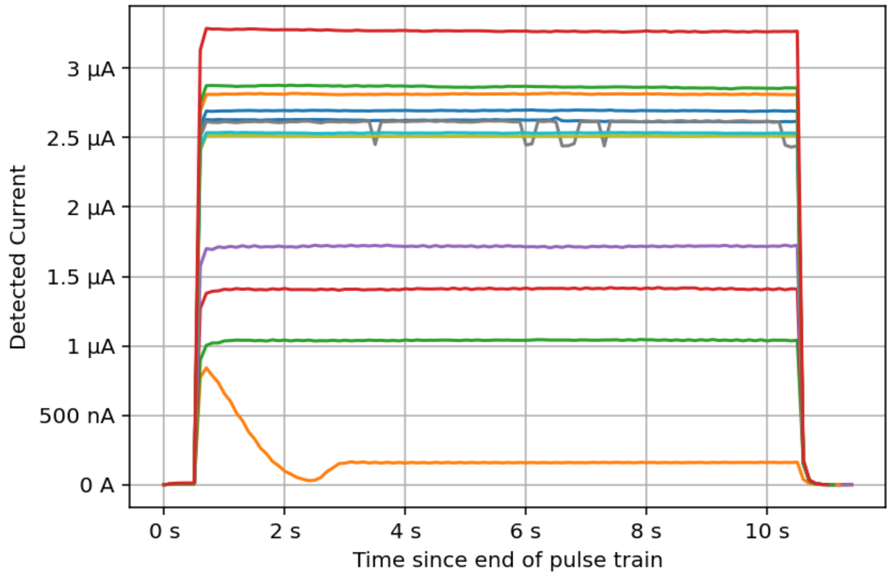

Figure 43: Detected current by capAccurate over time, for each pulse train

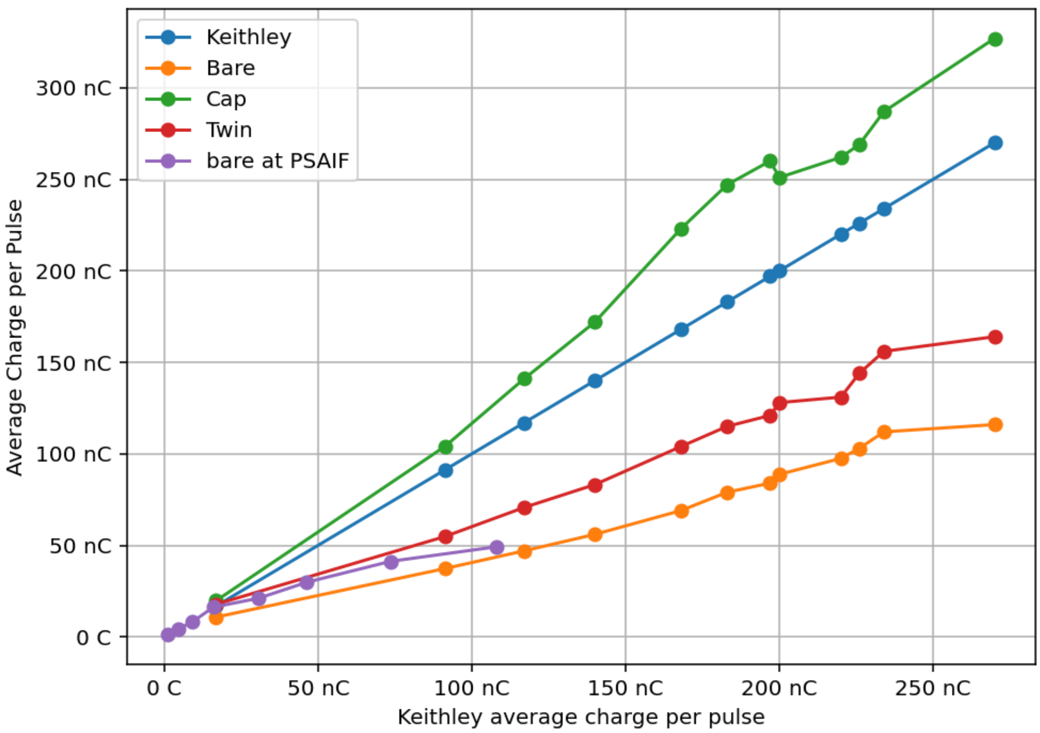

Figure 44: Detected charge per pulse w.r.t the reference electrometer, at IRA

Accurate-based device to detect *more* charges than the one injected in pulsed regime[12], which raises questions concerning the reference electrometer. This particular effect could partially be explained by the fact that the internal capacitance of the Keithley (max $2\,\mu C$) "folded" (had to be reset) during the pulse train, as it was getting overloaded. It however cannot explain the fact that capAccurate detected 17% more charge for the first datapoint, which is a datapoint where

[12]neglecting the overshoot, which is not what is happening based on figure 45

no folding occurred in the reference electromenter[13], particularly given its proper calibration, as shown in figure 35. This may put the adequacy of the reference electrometer for pulsed current into question, but a lot more testing would be needed, particularly given the fact that this is interpreted from an experimental device, in conditions not quite well defined. It however strongly suggest to avoid folding in the future.

A hint of what is happening can be found looking at the end of the pulse train, as reported by capAccurate in figure 45. Note that the first point has been removed, because it may still be in the pulse depending on the synchronization between Accurate and the accelerator. It can be noted that the system takes a few hundred milliseconds to reach steady state again. This shows that the ionization chamber may take significantly more time to fully absorb a pulse than previously thought, and thus that an individual pulse may not be independent from the others depending on the repetition frequency. This phenomenon might by the cause of the strange shape of the lower curve in figure 43. The first few pulses may be well collected, before saturating the chamber, reducing the collection efficiency, before finding a steady state. With higher dose per pulse, the saturation may happen much more quickly, and reach steady state faster. One can also note that the first current point in the pulse should be on average half the steady state value, as Accurate and the accelerator are not synchronized. For all curves, the first point is always very close to the steady state value, hinting that the first few pulses in the pulse train may yield more generation of charges.

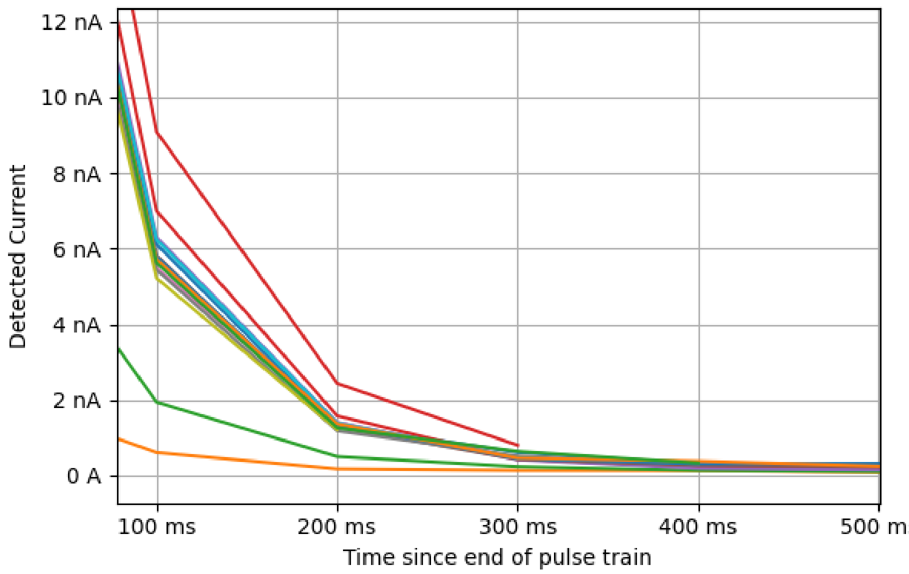

Figure 45: Reported current by capAccurate at the end of the pulse train, for all datasets

The relation between the detected charge per pulse for each device with respect to the dose detected by the Advanced Markus chamber is shown in figure 46. It is interesting to note that, even if the measurements between the Keithley and Accurate-based devices show a linear relationship with one another, they have a clear saturating behaviour with the Advanced Markus readings. This should come from the above explained saturation of the ionization chamber due to the pulse train, as there is no clear linear relationship seen between dose and collected charge below $100\,\mathrm{nC}$ as can be found in [15].

[13]The Keithley 6517B detected $1.68\,\mu\mathrm{C}$, which is smaller that the upper limit before folding of $2\,\mu\mathrm{C}$

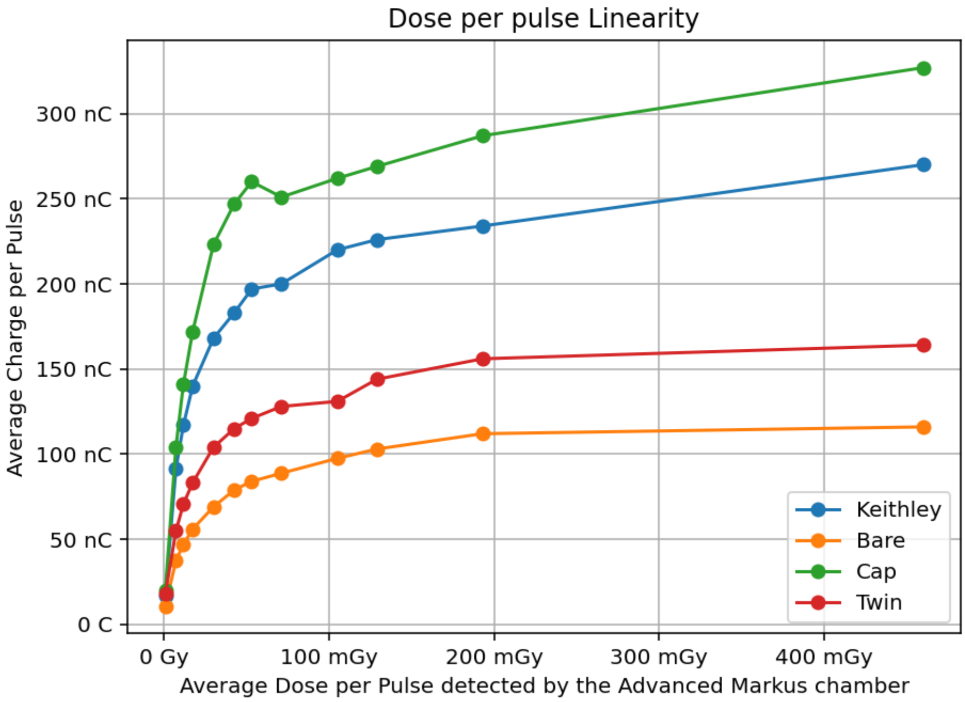

Figure 46: Average detected charge per pulse w.r.t the dose detected by the Advanced Markus chamber

6.3.4 An Electrical Approach to Ionization Chambers in Pulsed Regime

The aim of this section is to look at the behaviour of the IG5 ionization chamber from an electrical point of view. This means that while some inspiration may be taken from the possible physics of the chamber, it will be considered as a black box.

This experiment could not be done during the initial slot, as time had ran out. Thus, the values presented here were made a few days later in parasitic mode[14], using a different, experimental accelerator with a pulse width in the order of the µs. Because of this, only a single charge per pulse could be tested ($\approx 300\,\mathrm{nC}$), with a single pulse.

The electrical setup used is shown in figure 47. The ionization chamber was placed inline with the beam, behind the primary experiment. Different resistors were then placed in parallel with the oscilloscope (R_1) and the waveform for a single pulse recorded. The capacitance C_{cable} is roughly equal to $2.9\,\mathrm{nF}$.

Before trying to find a model, let us look at the raw data. First, one to see some kind of a transient, which will bring the initial voltage of $0\,\mathrm{V}$ to a certain value. If R_1 is big, one would expect to always find the same voltage at the end of the change, as the charges would not have time to escape during this initial step. The duration of this transient ought to be at least in the order of microseconds, as the pulse width of the accelerator is in this range. Once the transient has ended, one should see an exponential decrease due to C_{cable} and R_1. It is however possible for the ionization chamber to still be active and to see a residual current generated. Due to the biasing voltage, one can expect this residual current to only be negative. After some time has passed, the voltage read on the oscilloscope must read arbitrarily close to $0\,\mathrm{V}$, due to conservation of energy.

The decimated data normalized over the maximum voltage of the sample for better readability

[14]They were made while other people had control of the accelerator

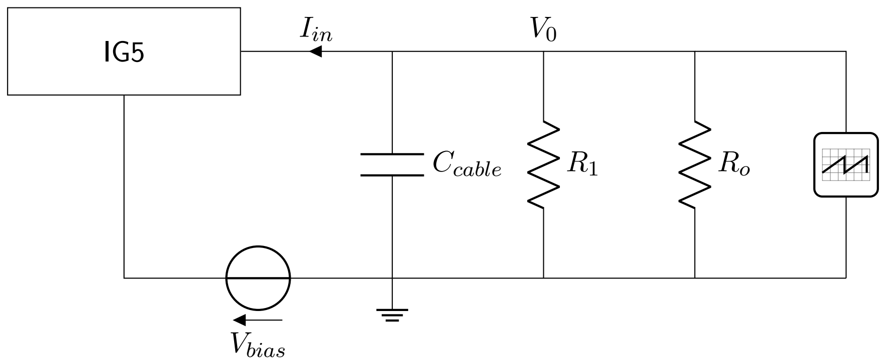

Figure 47: Setup for the oscilloscope measurements, with C_{cable} the capacitance of the cable, R_1 an arbitrary resistor and R_o the resistance of the oscilloscope.

can be found in figure 48. The data had to be decimated due to the high sampling rate of the oscilloscope, which caused unmanageable amount of data for a recording a few seconds long. One can note the initial transient, which lasts for $\sim 15\,\mu s$. This is significantly higher than the activity of the accelerator of $\sim 4\,\mu s$. After that, a exponential-like decrease can be seen. It is also worth noting that the higher R_1, the longer it takes to reach the maximum value. This may be explained by the fact that the higher R_1, the higher the voltage drop against V_{bias}, and thus the harder it is for the charges inside the ionization chamber to reach the electrodes.

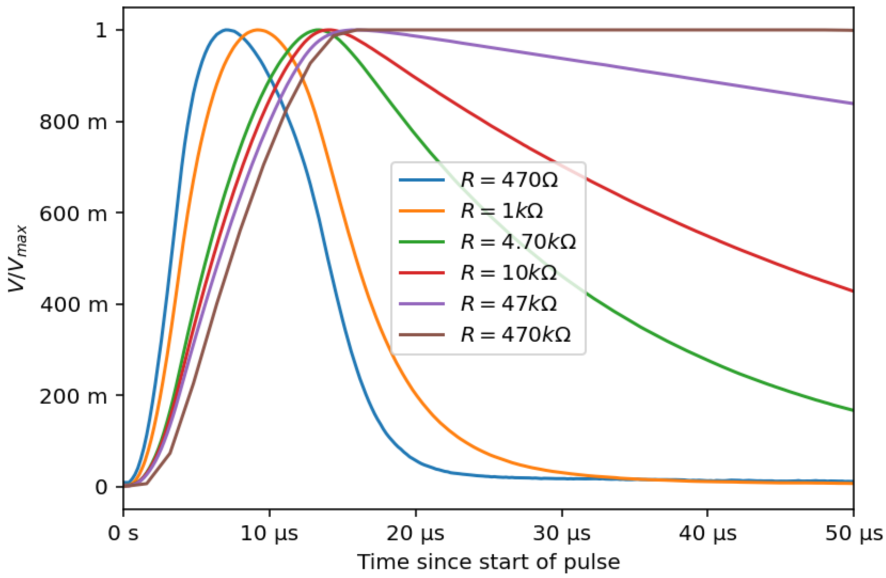

Figure 48: Decimated data recorded by the oscilloscope, normalized over the maximum voltage of the sample.

One can also extract I_{in} from the raw data. Let us define $R = (R_1//R_o)$. Then:

$$I_{in} = -I_{C_{cable}} - I_R \tag{52}$$

$$I_{in} = V_0' C_{cable} - V_0/R \tag{53}$$

The derived current curves are found in figure 49. The data as been scaled in time for visualization's sake with $\tau_{sys} = RC_{cable}$. One can see that after a very fast increase in current, an exponential-shape decrease is happening. After that, a plateau is reached, which *has* to come back to $0V$, but is very slow to do so.

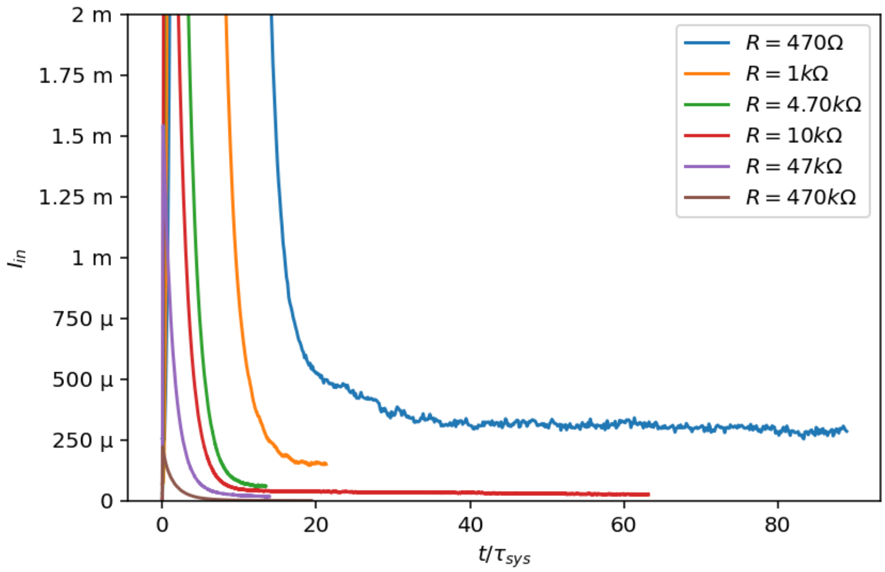

Figure 49: I_{in} extracted from oscilloscope reading

Delta Discharge Let us first consider the case were the ionization chamber is considered to be a perfect current source. If that were the case, the discharge would be instantaneous[15] charging C_{cable}, and then reach steady state by discharging through R_o and R_1. This implies that, ultimately, the same time constant $\tau_{sys} = C_{cable} \cdot (R_1 // R_o)$ should be seen on all curves.

In order to test this hypothesis, each recording was first cropped by $15\,\mu s$ to remove all possible transient effects. It was then normalized in time w.r.t its corresponding τ_{sys}, and normalized in voltage w.r.t its maximum voltage. If the hypothesis is correct, then all curves should overlap each other, following an exponential decrease e^{-t}. Results are shown in figure 50.

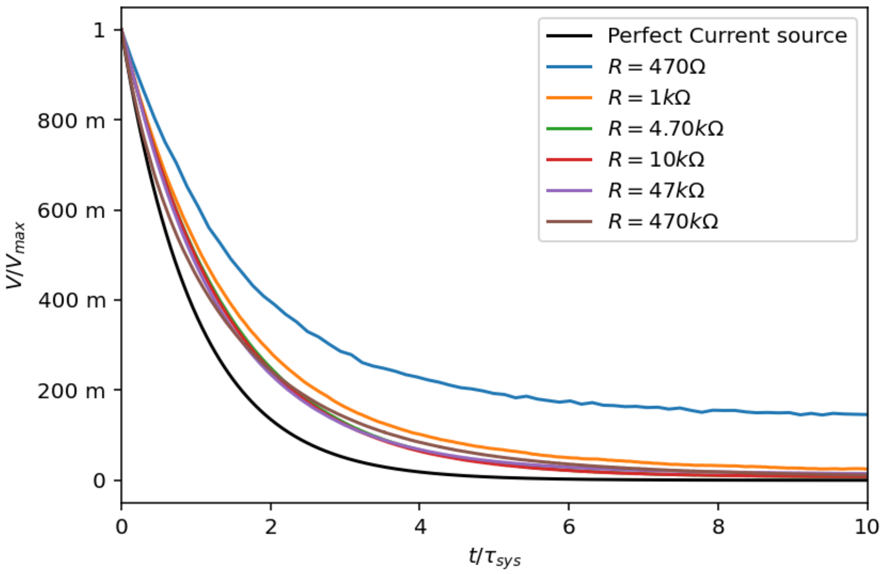

Figure 50: Ionization chamber response when connected to a parallel resistor R_1 and an oscilloscope, normalized in time with τ_{sys} and in voltage with the corresponding maximum value

[15] To the extend that the activity of the beam can be considered instantaneous

It can be seen that, except for very low resistance values, the decrease indeed follow an exponential initially, but with a larger time constant than τ_{sys}. Moreover, the difference between the true initial time constant with τ_{sys} is close to linear with R_1C_{cable}, which explains why an overlap is seen on the graph, despite resistance values spanning a few decades. This may be explained by the fact that the higher the resistance, the higher the voltage drop over the oscilloscope working against V_{bias} and the less the efficiency of the ionization chamber. Moreover, one can note that instead of reaching zero rapidly, as would be expected with an exponential decrease, a much slower phenomenon can be seen at the tail of the curve, showing almost as a constant offset. Unsurprisingly, the setups with a low time constant have a lower maximum voltage, and shorter τ_{sys}, which explains why the slow behaviour is more prevalent in these cases.

Scaled Time Constant Given the previous results, the first thing to do would be to find a scaling α in time so that the fast decrease portion of the curves match $e^{\frac{-t}{\alpha C_{cable}(R_O//R_1)}}$. Doing a least square fitting where this fast discharge is prevalent ($R_1 = 4.7\,\mathrm{k\Omega}$ and above), figure 51 is obtained with $\alpha = 1.43$. Note that this α constant is most likely dependant on the charge per pulse. More data is needed to explore this possibility.

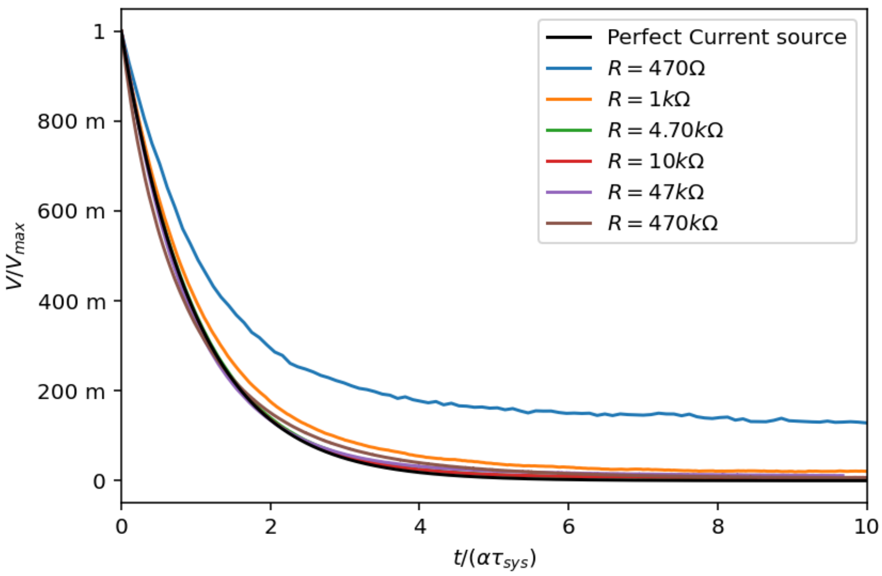

Figure 51: Normalized response of the ionization chamber, with time scaling α

In electrical terms, this could seem to be easily represented with an additional capacitor in parallel with value $C_{add} = (1-\alpha)C_{cable}$. However, this would imply that the higher the resistance, the lower the maximum voltage drop. This is disproven in figure 52a, which show that the maximum voltage gets higher with resistance despite collecting less charges overall, as shown in figure 52b. Additionally, one can see that even if it seems at first glance that all charges are contained inside of the "fast" discharge, the integrated charge continues to grow well after its time constant, making it hard to judge when to stop recording during experimentation.

This behaviour may thus be better modelled by using an additional current source, as proposed below.

Additional Current Source Let us consider the following equivalent diagram, the ionization chamber being modelled as three current sources:

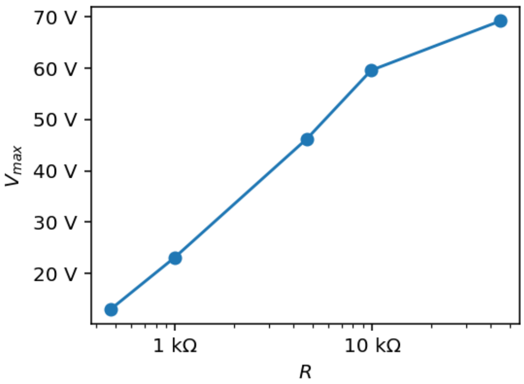

(a) Maximum voltage drop w.r.t R

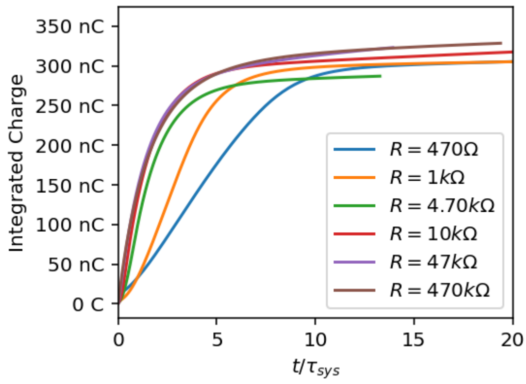

(b) Integrated Charge over time

Figure 52: Maximum voltage and integrated charge

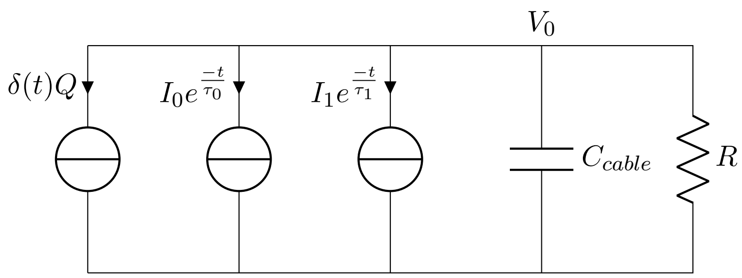

Figure 53: Ionization chamber modelled as a combination of current sources

Since the transient is very complicated to model, it will be considered that time starts after the end of the transient, with C_{cable} holding the remaining charge Q. The first current source, with parameters I_0 and τ_0 will model the fast exponential decrease, while the second one, with parameters I_1 and τ_1 will model the slower exponential.

One can derive the following:

$$I_0 e^{\frac{-t}{\tau_0}} + I_1 e^{\frac{-t}{\tau_1}} + \dot{V}_0 C_{cable} + V_0/R = 0 \qquad (54)$$

$$V_0(t) = k e^{\frac{-t}{\tau_{sys}}} + \frac{I_0 \tau_{sys} R \tau_0 e^{\frac{-t}{\tau_0}} - I_0 R \tau_0 \tau_1 e^{\frac{-t}{\tau_0}} + I_1 \tau_{sys} R \tau_1 e^{\frac{-t}{\tau_1}} - I_1 R \tau_0 \tau_1 e^{\frac{-t}{\tau_1}}}{(\tau_{sys} - \tau_0)(\tau_{sys} - \tau_1)} \qquad (55)$$

$$V_0(0) = Q/C \qquad (56)$$

This approach yields no interesting results, as it fails to fit the data properly.

Wrapping Up It is seen above that the behaviour of the ionization chamber is highly non-linear w.r.t the resistance connected at its end, even without taking into account different charge per pulse, which is also a nonlinear phenomenon in many regards. This causes trouble to extract reasonable metrics from the measurements, because there seem to not be a particular relationship between R and the input current shape, as well as the total collected charge.

Moreover, this raises the question of the influence of measurement equipment over the total charge collected. While previous experiments[17] have shown that the effect of a $50\,\mathrm{M\Omega}$ resistor at the input of Accurate has no significant impact on the charge generated by the ionization chamber[16] for pulses less than $100\,\mathrm{nF}$, above results show that differences in at least tens of percent can be expected. This is reinforced by the fact that it should be physically impossible to collect more charge than $V_{bias} \cdot C_{in}$ for a sufficiently large resistor, as the voltage drop on the capacitor would reach the biasing voltage, thus reducing the electric field driving the collection of charges to zero.

The Keithley 6517B specifications unfortunately do not mention the transconductance nor the bandwidth of their integrating OTA, even though there has to be an upper limit in the dose per pulse at which a significant voltage drop may be seen at its input. Using a second Keithley 6517B[17] in voltage mode in parallel to a current measuring one during a pulse could help evaluate the likelihood of the reference equipment having a detrimental effect on the ionization chamber. This result also give another strong advantage to using large input capacitance, as reducing the voltage drop at the input not only improve the accuracy of Accurate, but may also reduces the effect of its imperfections on the ionization chamber.

While it as been shown that the pulse can reasonably be modelled as a delta discharge as a first approximation to model a single discharge, many questions remain. The behaviour of the transient may be important, as its duration is not negligible in front of Accurate's cycle time. Also, some evidence has been presented showing that a low frequency phenomenon may be happening inside of the chamber, lasting potentially hundreds of millisecond. As train of pulses are a common occurrence at CERN, a proper physical model of the ionization chamber would be greatly useful.

Moreover, it would be interesting to set up a new comparison metrics based an Kronecker's delta discharge implemented with a capacitor in the order of the nanofarad[18], thus providing an accelerator and ionization chamber agnostic value, making testing much more flexible, repeatable, consistent and easy.

6.4 Single Pulse Evaluation

During the same parasitic measurement slot as the oscilloscope recordings, a short time window was allocated for making single pulse measurement with the same accelerators parameters throughout, but changing the location of the ionization chamber. Some of the testing locations are shown in 54.

A single pulse was then recorded for the Keithley 6517B, as well as bareAccurate and capAccurate. During the experiment, a lack of confidence about the electrometer was felt, as its readout was not in agreement with the other test devices. This unit was thus exchanged with another Keithley 6517B for the last measurements. Due to time constraints, it was not possible to perform the experiment again for that device.

The results are shown in table 5.

First, one can see that bareAccurate and capAccurate reported close values for all measurements except when exposed in the beam, with an average difference of 9.5%, which is in accordance with the offset measured at the Calibration Laboratory for static currents. CapAccurate then detected more than $2\times$ more charge than bareAccurate, confirming that the increased capacitance is beneficial for Accurate in saturation regime.

Then, it can be seen that the original Keithley 6517B reported values ten times lower than the other two devices. The replacement one's value was very close to the one measured by the other two devices for the measurement in front of the machine, and also zero for the control room.

[16] though these measurements were made with a $2.9\,\mathrm{nF}$ cable

[17] The Keithley 6517B has a very high input resistance ($100\,\mathrm{T\Omega}$) for voltage measurements

[18] comparable to cable parasitic capacitance

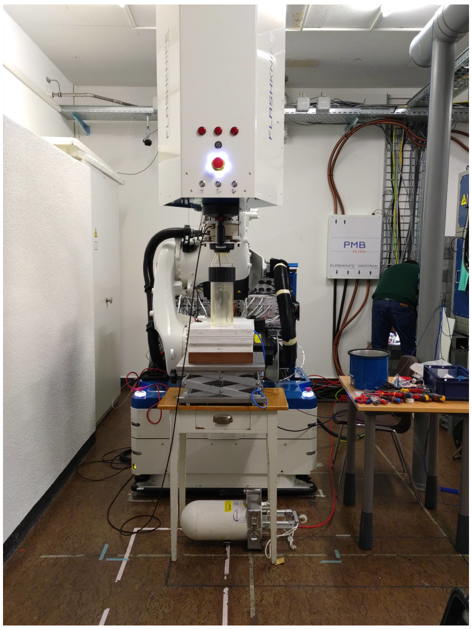

(a) Ionization chamber below the beam

(b) Ionization chamber above the beam

Figure 54: Pictures some ionization chamber location

Position	Keithley 6517B	bareAccurate	capAccurate
Below Beam	117 nC	140 nC	305 nC
Above Beam	1.00 nC	10.0 nC	11.2 nC
In front of the machine	2.67 nC	2.58 nC	2.79 nC
On the machine	300 pC	2.50 nC	2.72 nC
Behind the machine	110 pC	900 pC	981 pC
In Control Room	0 fC	0 fC	0 fC

Table 5: Integrated charge of single pulse measurement, with different ionization chamber's location. Keithley 6517B was changed for measurements in the control room and in front of the machine.

Moreover, when looking at the data presented in figure 55, it is clear that the original Keithley was miss-behaving. It does not really register the pulse, but instead shows a quasi constant current, which is not what the second one, nor capAccurate is doing. Moreover, this trend can been seen in all other measurements done with the original device. This malfunction may explain the poor results obtained at the Calibration Laboratory, initially attributed to human error, as well as the lower recorded charge per pulse in section 6.3.3. This device should not be used before extensive testing is done to insure that this particular unit is working within specified tolerances.

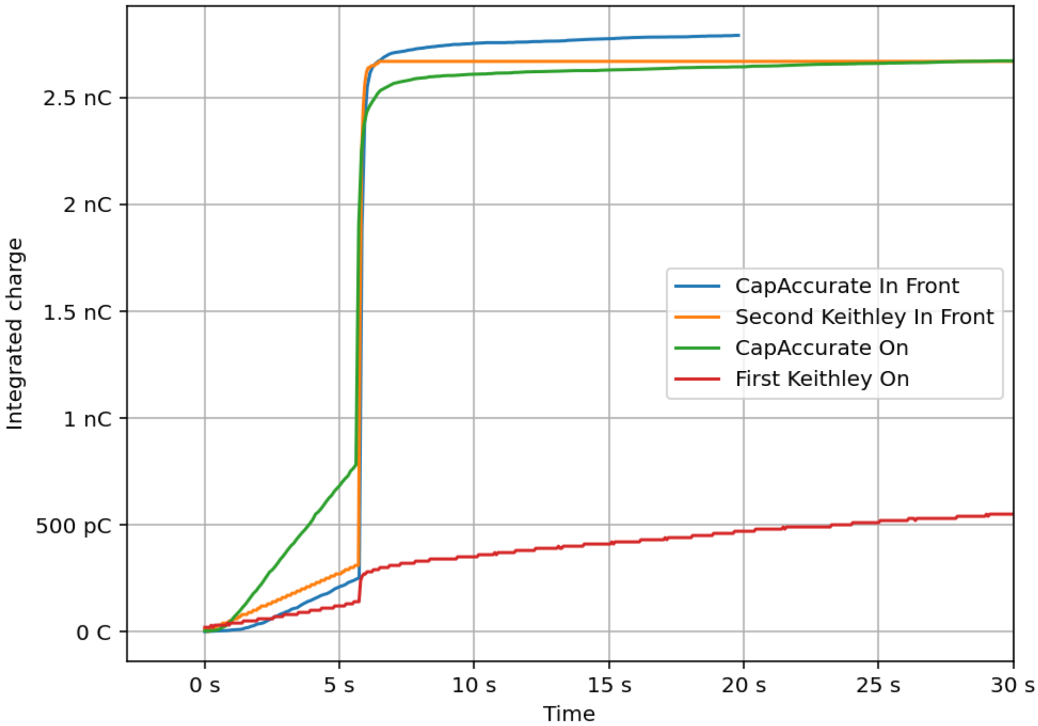

Figure 55: Comparison between charges collected by capAccurate, as well as first and second Keithley 6517B. Position relative to the machine.

7 Conclusion and Outlook

This thesis presents improvements of an ultra-wide dynamic range current digitizer ASIC with better than the state-of-the-art sensitivity in the area of pulsed current, as well as its integration into a complete radiation protection system, CROME. The introduction presented a summary of CERN's accelerator complex and outlined the need for versatile radiation monitoring devices, capable of accurately measuring static and pulsed ionizing radiation. In addition, CROME, the current radiation monitoring system from RP at CERN was presented. The behaviour and operation of its sensor, an ionization chamber, was covered, as well as the challenges in accurate measurements of radiation dose in both linear range and pulsed regime. The complexity of its discrete component-based front-end was put forward in both maintaining and upgrading such systems. An in-house developed ASIC solution simplifies the process while providing known performance, thus justifying the replacement of current system with a single chip solution for future systems.

Accurate 2, the last generation of prototype was presented in the previous chapter, as well as methods for modelling its behaviour in both static and pulsed regime. It was demonstrated that under a light set of assumptions, increasing input capacitance results in increased performance for pulsed fields, as well as potential for higher end of the linear range to be increased, through a shortening of the charge pumps' connection time. In addition, challenges regarding the use of direct slope measurement method in combination with the current measurement method (charge balancing) in the higher end of the linear range was presented.

Additional modelling aimed at probing the potential for different input topologies using real components were performed in chapter 3. It was found that the insulation resistance in combination with the offset error of the OTA were the crucial limiting factors to use discrete capacitors on the input path.

Based on this knowledge, the design of a new PCB prototype allowing for different input circuitry and the use of multiple ASICs was made and presented in chapter 4. Precautions were taken in the design of the input path to minimize leakage with the use of guard traces, removal of conformal coating and shielding.

CROME's software was modified to integrate the new prototype, as well as to allow its use on a development board, which does not include all of the devices present in the production system. This implied a quantity of changes in the front-end module, but also more generally in the project, going to the software running on the linux side of the Zynq SoC. In addition, some changes were suggested in the front-end's HDL designed which could increase the resolution in low currents as well as improve the behaviour of multi ASICs designs.

In chapter 6, the prototype was tested at different facilities to evaluate its performance in both static and pulsed regime. It showed excellent performance in the linear range, with a slightly increased leakage of $\sim 70\,\mathrm{fA}$, which can be greatly reduced by reducing the capacitor's value or the offset error of the OTA. Tests at IRA were met with technical issues putting the model of the ionization chamber in pulsed regime into question. The prototype nonetheless detected much more charges than the original device, indicating a good potential. An approach to the modelling of ionization chamber in pulsed regime from an electronics point of view was attempted and showed that complex, non-linear behaviours happens with respect to the components connected at its output, even for a constant dose per pulse. It was shown that a Kronecker's delta discharge was satisfactory in many regards, but lacked the capacity to explain lower frequency phenomenons, which may become dominant in the case of train of pulses. A new comparison metric was suggested allowing more robust and easy comparison, as the accelerator and ionization chamber's choice and parameters may impact the accuracy of the device and produce inconsistent results, as demonstrated with the test campaign.

The research towards Accurate 3 will continue, strengthened by the above mentioned discoveries. The ASIC will act as the strong pillar supporting the future radiation monitoring at CERN, thus safeguarding the personnel by ensuring a safe and secure working environment for the countless innovations and discoveries to be made at this wonderful scientific laboratory.

References

[1] R. Steerenberg, M. Albert, R. Alemany-Fernández, *et al.*, "Operation and Performance of the Cern Large Hadron Collider During Proton Run 2," en, *Proceedings of the 10th Int. Particle Accelerator Conf.*, vol. IPAC2019, 4 pages, 0.255 MB, 2019, Artwork Size: 4 pages, 0.255 MB ISBN: 9783954502080 Medium: PDF Publisher: JACoW Publishing, Geneva, Switzerland. DOI: 10.18429/JACOW-IPAC2019-MOPMP031. [Online]. Available: http://jacow.org/ipac2019/doi/JACoW-IPAC2019-MOPMP031.html (visited on 03/15/2022).

[2] E. A. Mobs, *The CERN accelerator complex*, en, Number: OPEN-PHO-ACCEL-2016-013, Aug. 2018. [Online]. Available: https://cds.cern.ch/record/2225847 (visited on 03/15/2022).

[3] K. Hanke, "Past and Present Operation of the CERN PS Booster," en, *International Journal of Modern Physics A*, vol. 28, no. 13, p. 1 330 019, May 2013, ISSN: 0217-751X, 1793-656X. DOI: 10.1142/S0217751X13300196. [Online]. Available: https://www.worldscientific.com/doi/abs/10.1142/S0217751X13300196 (visited on 03/15/2022).

[4] A. Lombardi, *LINAC4 Commissioning*, en, Number: CERN-ACC-2018-196 Pages: TH1P01, 2018. DOI: 10.18429/JACoW-LINAC2018-TH1P01. [Online]. Available: https://cds.cern.ch/record/2669232 (visited on 03/15/2022).

[5] A. Newborough, "IEEE : The Upgrade of the CERN Proton Synchrotron Booster Transfer Line Magnets," en, *IEEE Trans. Appl. Supercond.*, vol. 30, p. 4 000 405, 2020. DOI: 10.1109/TASC.2020.2967334. [Online]. Available: https://cds.cern.ch/record/2744551 (visited on 03/15/2022).

[6] K. H. Lieser, *Nuclear and Radiochemistry: Fundamentals and Applications*. Weinheim, Germany: Wiley-VCH Verlag GmbH, Jun. 1997, ISBN: 978-3-527-61289-5. [Online]. Available: http://doi.wiley.com/10.1002/9783527612895 (visited on 03/16/2022).

[7] G. F. Knoll, *Radiation detection and measurement*, 3rd ed. New York: J. Wiley, 2000, ISBN: 978-0-471-07338-3.

[8] D. Forkel-Wirth, S. Roesler, M. Silari, *et al.*, *Radiation protection at CERN*, eng. Geneva: CERN, 2013.

[9] H. Boukabache, C. Toner, D. Perrin, and G. Ducos, "Fault Resilient FPGA Design for 28nm ZYNQ SoC based Radiation Protection Instrumentation Fulfilling Safety Integrity Level 2," in *European Symposium on Reliability of Electron Devices, Failure Physics and Analysis*, 2019.

[10] R. Schmidt, R. Assmann, E. Carlier, *et al.*, "Protection of the CERN Large Hadron Collider," en, *New Journal of Physics*, vol. 8, no. 11, pp. 290–290, Nov. 2006, Publisher: IOP Publishing, ISSN: 1367-2630. DOI: 10.1088/1367-2630/8/11/290. [Online]. Available: https://doi.org/10.1088/1367-2630/8/11/290 (visited on 03/15/2022).

[11] F. Bordry, R. Schmidt, K. H. Mess, F. Rodríguez-Mateos, B. Puccio, and R. Denz, *Machine Protection for the LHC : Architecture of the Beam and Powering Interlock Systems*, en, Number: LHC-Project-Report-521, Dec. 2001. [Online]. Available: https://cds.cern.ch/record/531820 (visited on 03/15/2022).

[12] M. Gotz, "Dosimetry of Highly Pulsed Radiation Fields," HZDR, Germany, Tech. Rep.

[13] B. B. Rossi and H. H. Staub, *Ionization Chambers and Counters*. New York: McGraw-Hill, 1949.

[14] J. W. Boag, E. Hochhäuser, and O. A. Balk, "The effect of free-electron collection on the recombination correction to ionization measurements of pulsed radiation," *Physics in Medicine and Biology*, vol. 41, no. 5, pp. 885–897, May 1996, ISSN: 0031-9155, 1361-6560. DOI: 10.1088/0031-9155/41/5/005. [Online]. Available: https://iopscience.iop.org/article/10.1088/0031-9155/41/5/005 (visited on 03/16/2022).

[15] A. Muller, "Réponse des Chambres d'Ionization dans des Champs de Radiation Pulsées Intenses," CERN, Tech. Rep., Jan. 2004. [Online]. Available: https://edms.cern.ch/ui/#!master/navigator/document?D:1961265955:1961265955:subDocs (visited on 12/02/2021).

[16] E. Voulgari, F. Krummenacher, F. Anghinolfi, M. Noy, and M. Kayal, "Utopia: A Nine Decade Femtoampere Sensitivity Current Digitizer and its Application in Ionizing Radiation Monitoring," en, *IEEE Trans. Nucl. Sci.*, vol. 65, p. 932, 2018. DOI: 10.1109/TNS.2018.2803339. [Online]. Available: https://cds.cern.ch/record/2643837 (visited on 03/16/2022).

[17] S. K. Mohanan, "An Accurate Ultra-low Current Measurement ASIC for Ionization Chamber Readout," Ph.D. dissertation, Wuppertal, Germany, Aug. 2021.

[18] P. Dawkins, *Differential Equations - Solutions to Systems*, Nov. 2020. [Online]. Available: https://tutorial.math.lamar.edu/Classes/DE/SolutionsToSystems.aspx (visited on 03/16/2022).

[19] S. K. Mohanan, H. Boukabache, V. Cruchet, D. Perrin, S. Roesler, and U. Pfeiffer, "An Ultra Low Current Measurement Mixed-Signal ASIC for Radiation Monitoring Using Ionisation Chambers," *IEEE Sensors Journal*, pp. 1–1, 2021, Conference Name: IEEE Sensors Journal, ISSN: 1558-1748. DOI: 10.1109/JSEN.2021.3132498.

[20] F. Pozzi, "CERN Radiation Protection (RP) calibration facilities," en, Number: CERN-THESIS-2015-394 Publication Title: CERN Document Server, Ph.D. dissertation, CERN, Mar. 2017. [Online]. Available: https://cds.cern.ch/record/2256137 (visited on 03/11/2022).

[21] M. Jaccard, M. T. Durán, K. Petersson, *et al.*, "High dose-per-pulse electron beam dosimetry: Commissioning of the Oriatron eRT6 prototype linear accelerator for preclinical use," *Medical Physics*, vol. 45, no. 2, pp. 863–874, Feb. 2018, ISSN: 2473-4209. DOI: 10.1002/mp.12713.

[22] M. Tavlet and M. Leon Florian, "PSAIF: The PS-ACOL irradiation facility at CERN," in *RADECS 91 First European Conference on Radiation and its Effects on Devices and Systems*, Sep. 1991, pp. 582–585. DOI: 10.1109/RADECS.1991.213533.

A Numerical Values

Name	Numerical Value
g_m	$3\,\mathrm{mS}$
V_{cp}	$2.5\,\mathrm{V}$
C_f	$4\,\mathrm{pF}$
R_{cp}	$200\,\Omega$
C_{cp}	$500\,\mathrm{fF}$
C_{cp_1}	$500\,\mathrm{fF}$
C_{cp_2}	$1\,\mathrm{pF}$
C_{cp_3}	$4\,\mathrm{pF}$
$I_{OTA_{max}}$	$140\,\mu\mathrm{A}$
T_{cycle}	$150\,\mathrm{ns}$

B Detailed solution for bareAccurate in static operation, during the Charge Pump Connection

$$\begin{bmatrix} V_{OTA_{in}}(t) \\ I_{cp}(t) \end{bmatrix} = k_1 \vec{\eta_1} e^{\frac{-t}{\gamma_1}} + k_2 \vec{\eta_2} e^{\frac{-t}{\gamma_2}} + \vec{x_p} \tag{57}$$

$$\gamma_1 = \frac{2C_{cp}C_{in}R_{cp}}{C_{cp}R_{cp}g_m + C_{cp} + C_{in} + \sqrt{C_{cp}^2R_{cp}^2g_m^2 + 2C_{cp}^2R_{cp}g_m + C_{cp}^2 - 2C_{cp}C_{in}R_{cp}g_m + 2C_{cp}C_{in} + C_{in}^2}} \tag{58}$$

$$\gamma_2 = \frac{2C_{cp}C_{in}R_{cp}}{C_{cp}R_{cp}g_m + C_{cp} + C_{in} - \sqrt{C_{cp}^2R_{cp}^2g_m^2 + 2C_{cp}^2R_{cp}g_m + C_{cp}^2 - 2C_{cp}C_{in}R_{cp}g_m + 2C_{cp}C_{in} + C_{in}^2}} \tag{59}$$

$$\vec{\eta_1} = \begin{bmatrix} -\frac{C_{in}R_{cp}}{g_1g_m} + \frac{1}{g_m} + \frac{C_{in}}{C_{cp}g_m} \\ 1 \end{bmatrix} \tag{60}$$

$$\vec{\eta_2} = \begin{bmatrix} -\frac{C_{in}R_{cp}}{g_2g_m} + \frac{1}{g_m} + \frac{C_{in}}{C_{cp}g_m} \\ 1 \end{bmatrix} \tag{61}$$

$$k_1 = A_1\epsilon + B_1 \tag{62}$$

$$A_1 = -\frac{g_1\left(C_{cp}C_{in}R_{cp} - C_{cp}R_{cp}g_2g_m - C_{cp}g_2 - C_{in}g_2\right)}{C_{cp}C_{in}R_{cp}^2\left(g_1 - g_2\right)} \tag{63}$$

$$B_1 = \frac{g_1\left(I_{in} - V_{cm}g_m + V_{cp}g_m\right)\left(C_{cp}C_{in}R_{cp} - C_{cp}g_2 - C_{in}g_2\right)}{C_{cp}C_{in}R_{cp}^2g_m\left(g_1 - g_2\right)} \tag{64}$$

$$k_2 = A_2\epsilon + B_2 \tag{65}$$

$$A_2 = -\frac{g_1\left(C_{cp}C_{in}R_{cp} - C_{cp}R_{cp}g_2g_m - C_{cp}g_2 - C_{in}g_2\right)}{C_{cp}C_{in}R_{cp}^2\left(g_1 - g_2\right)} \tag{66}$$

$$B_2 = -\frac{g_2\left(I_{in} - V_{cm}g_m + V_{cp}g_m\right)\left(C_{cp}C_{in}R_{cp} - C_{cp}g_1 - C_{in}g_1\right)}{C_{cp}C_{in}R_{cp}^2g_m\left(g_1 - g_2\right)} \tag{67}$$

$$\vec{x_p} = \begin{bmatrix} V_{cm} - \frac{I_{in}}{g_m} \\ 0 \end{bmatrix} \tag{68}$$

C Detailed solution for capAccurate in static operation, during the Charge Pump Connection

$$\begin{bmatrix} V_{OTA_{in}}(t) \\ I_{cp}(t) \end{bmatrix} = k_1 \vec{\eta_1} e^{\frac{-t}{\gamma_1}} + k_2 \vec{\eta_2} e^{\frac{-t}{\gamma_2}} + \vec{x_p} \tag{69}$$

$$\gamma_1 = \frac{2C_{cap}C_{cp}R_{cap}R_{cp}}{\beta} \tag{70}$$

$$\gamma_2 = \frac{2C_{cap}C_{cp}R_{cap}R_{cp}}{\beta_2} \tag{71}$$

$$\beta_1 = C_{cap}R_{cap} + C_{cp}R_{cap}R_{cp}g_m + C_{cp}R_{cap} + C_{cp}R_{cp} + \sqrt{\mu} \tag{72}$$

$$\beta_2 = C_{cap}R_{cap} + C_{cp}R_{cap}R_{cp}g_m + C_{cp}R_{cap} + C_{cp}R_{cp} - \sqrt{\mu} \tag{73}$$

$$\mu_1 = C_{cap}^2R_{cap}^2 - 2C_{cap}C_{cp}R_{cap}^2R_{cp}g_m + 2C_{cap}C_{cp}R_{cap}^2 - 2C_{cap}C_{cp}R_{cap}R_{cp} + C_{cp}^2R_{cap}^2R_{cp}^2g_m^2 + 2C_{cp}^2R_{cap}^2R_{cp}g_m + C_{cp}^2R_{cap}^2 + 2C_{cp}^2R_{cap}R_{cp}^2g_m + 2C_{cp}^2R_{cap}R_{cp} + C_{cp}^2R_{cp}^2 \tag{74}$$

$$\vec{\eta_1} = \begin{bmatrix} \frac{R_{cap}(-C_{cap}C_{cp}R_{cp}+C_{cap}g_1+C_{cp}g_1)}{C_{cp}g_1(R_{cap}g_m+1)} \\ 1 \end{bmatrix} \tag{75}$$

$$\vec{\eta_2} = \begin{bmatrix} \frac{R_{cap}(-C_{cap}C_{cp}R_{cp}+C_{cap}g_2+C_{cp}g_2)}{C_{cp}g_2(R_{cap}g_m+1)} \\ 1 \end{bmatrix} \tag{76}$$

$$k_1 = A_1\epsilon + B_1 \tag{77}$$

$$A_1 = -\frac{g_1\left(C_{cap}C_{cp}R_{cap}R_{cp} - C_{cap}R_{cap}g_2 - C_{cp}R_{cap}R_{cp}g_2g_m - C_{cp}R_{cap}g_2 - C_{cp}R_{cp}g_2\right)}{C_{cap}C_{cp}R_{cap}R_{cp}^2\left(g_1 - g_2\right)} \tag{78}$$

$$B_1 = \frac{g_1\left(C_{cap}C_{cp}R_{cp} - C_{cap}g_2 - C_{cp}g_2\right)\left(I_{in}R_{cap} - R_{cap}V_{cm}g_m + R_{cap}V_{cp}g_m - V_{cm} + V_{cp} - \epsilon_1\right)}{C_{cap}C_{cp}R_{cp}^2\left(g_1 - g_2\right)\left(R_{cap}g_m + 1\right)} \tag{79}$$

$$k_2 = A_2\epsilon + B_2 \tag{80}$$

$$A_2 = \frac{g_2\left(C_{cap}C_{cp}R_{cap}R_{cp} - C_{cap}R_{cap}g_1 - C_{cp}R_{cap}R_{cp}g_1g_m - C_{cp}R_{cap}g_1 - C_{cp}R_{cp}g_1\right)}{C_{cap}C_{cp}R_{cap}R_{cp}^2\left(g_1 - g_2\right)} \tag{81}$$

$$B_2 = -\frac{g_2\left(C_{cap}C_{cp}R_{cp} - C_{cap}g_1 - C_{cp}g_1\right)\left(I_{in}R_{cap} - R_{cap}V_{cm}g_m + R_{cap}V_{cp}g_m - V_{cm} + V_{cp} - \epsilon_1\right)}{C_{cap}C_{cp}R_{cp}^2\left(g_1 - g_2\right)\left(R_{cap}g_m + 1\right)} \tag{82}$$

$$\vec{x_p} = \begin{bmatrix} \frac{-I_{in}R_{cap}+R_{cap}V_{cm}g_m+V_{cm}+\epsilon_1}{R_{cap}g_m+1} \\ 0 \end{bmatrix} \tag{83}$$

D Detailed solution for capAccurate in static operation, during the Current Integration

$$V_{OTA_{in}}(t) = V_{cm} - \frac{I_{in}}{g_m + 1/R_{cap}} + \frac{\epsilon_1/R_{cap}}{g_m + 1/R_{cap}} + \epsilon e^{\frac{-t}{\tau_{sys}}} \quad (84)$$

$$\tau_{sys} = \frac{C_{cap}}{g_m + 1/R_{cap}} \quad (85)$$

E IRA Additional Graphs

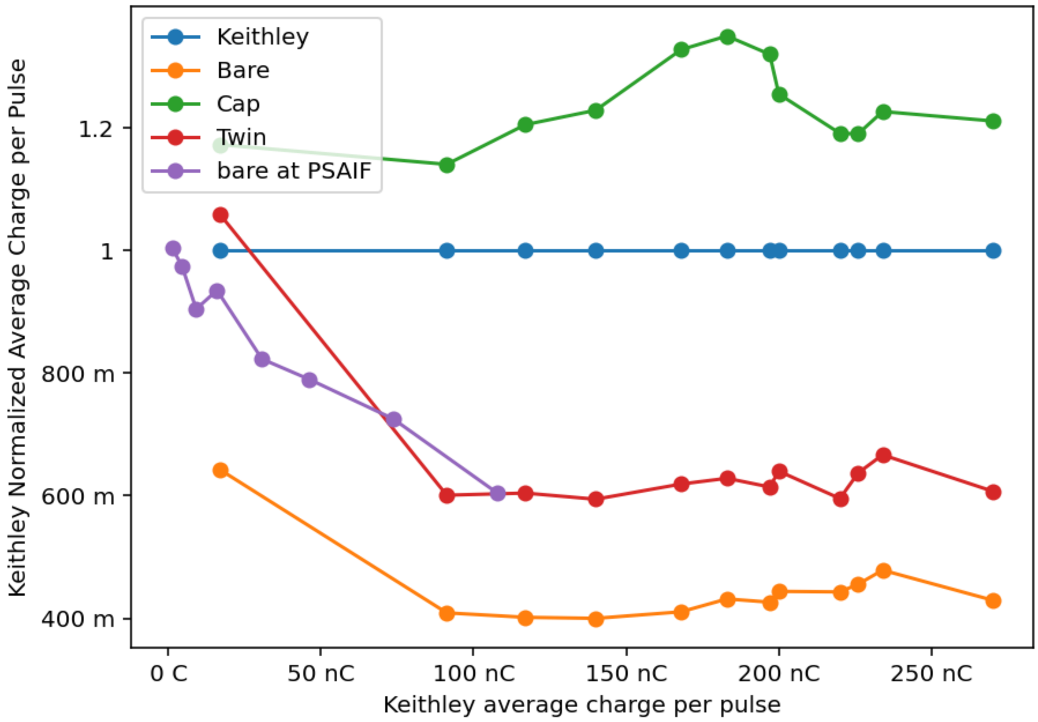

Figure 56: Detected charge per pulse, normalized over the reference electrometer